

# Studies of the Response of the Prototype CMS Hadron Calorimeter, Including Magnetic Field Effects, to Pion, Electron, and Muon Beams

V.V. Abramov<sup>ℓ</sup>, B.S. Acharya<sup>s</sup>, N. Akchurin<sup>s</sup>, I. Atanasov<sup>p</sup>,  
G. Baiatian<sup>q</sup>, A. Ball<sup>g</sup>, S. Banerjee<sup>r</sup>, S. Banerjee<sup>s</sup>,  
P. de Barbaro<sup>n</sup>, V. Barnes<sup>m</sup>, G. Bencze<sup>a</sup>, A. Bodek<sup>n</sup>,  
M. Boone<sup>i</sup>, H. Budd<sup>n</sup>, L. Cremaldi<sup>i</sup>, P. Cushman<sup>h</sup>,  
S.R. Dugad<sup>s</sup>, L. Dimitrov<sup>p</sup>, A. Dyshkant<sup>n</sup>, J. Elias<sup>c</sup>,  
V.N. Evdokimov<sup>ℓ</sup>, D. Fong<sup>g</sup>, J. Freeman<sup>c</sup>, V. Genchev<sup>p</sup>,  
P.I. Goncharov<sup>ℓ</sup>, D. Green<sup>c</sup>, A. Gurtu<sup>r</sup>, V. Hagopian<sup>d</sup>,  
P. Iaydjiev<sup>p</sup>, Yu. Korneev<sup>ℓ</sup>, A. Krnitsyn<sup>ℓ</sup>, G. Krishnaswami<sup>n</sup>,  
M.R. Krishnaswamy<sup>s</sup>, V. Kryshkin<sup>ℓ</sup>, S. Kunori<sup>g</sup>,  
A. Laasanen<sup>m</sup>, D. Lazic<sup>d</sup>, L. Levchuk<sup>f</sup>, L. Litov<sup>o</sup>,  
N.K. Mondal<sup>s</sup>, T. Moulik<sup>r</sup>, V.S. Narasimham<sup>s</sup>,  
A. Nemashkalo<sup>f</sup>, Y. Onel<sup>e</sup>, P. Petrov<sup>o</sup>, Yu. Petukhov<sup>b</sup>,

S. Piperov<sup>p</sup>, V. Popov<sup>f</sup>, J. Reidy<sup>i</sup>, A. Ronzhin<sup>c</sup>, R. Ruchti<sup>j</sup>,  
J.B. Singh<sup>k</sup>, Q. Shen<sup>m</sup>, A. Sirunyan<sup>q</sup>, A. Skuja<sup>g</sup>, E. Skup<sup>n</sup>,  
P. Sorokin<sup>f</sup>, K. Sudhakar<sup>r</sup>, D. Summers<sup>i</sup>, F. Szoncso<sup>a</sup>,  
S.I. Tereshenko<sup>l</sup>, C. Timmermans<sup>h</sup>, S.C. Tonwar<sup>r</sup>,  
L. Turchanovich<sup>l</sup>, V. Tyukov<sup>b</sup>, A. Volodko<sup>b</sup>, A. Yukaev<sup>b</sup>,  
A. Zaichenko<sup>l</sup>, A. Zatserklyaniy<sup>f</sup>

(The CMS-HCAL Collaboration)

<sup>a</sup>*CERN, Geneva, Switzerland*

<sup>b</sup>*Joint Institute for Nuclear Research, Dubna, Russia*

<sup>c</sup>*Fermi National Accelerator Laboratory, Batavia, IL 60510*

<sup>d</sup>*Florida State University, Tallahassee, FL 32306*

<sup>e</sup>*University of Iowa, Iowa City, IA 52242*

<sup>f</sup>*National Science Center Kharkov Institute of Physics and Technology, Kharkov,  
Ukraine*

<sup>g</sup>*University of Maryland, College Park, MD 20742*

<sup>h</sup>*University of Minnesota, Minneapolis, MN 55455*

<sup>i</sup>*University of Mississippi, University, MS 38677*

<sup>j</sup>*University of Notre Dame, Notre Dame, IN 46556*

<sup>k</sup>*Panjab University, Chandigarh, India*

<sup>ℓ</sup>*Institute for High Energy Physics, Protvino, Russia*

<sup>m</sup>*Purdue University, West Lafayette, IN 47907*

<sup>n</sup>*University of Rochester, Rochester, NY 14627*

<sup>o</sup>*University of Sofia, Sofia, Bulgaria*

<sup>p</sup>*Institute for Nuclear Research and Nuclear Energy, Sofia, Bulgaria*

<sup>q</sup>*Yerevan Physics Institute, Armenia*

<sup>r</sup>*EHEP Group, Tata Institute of fundamental Research, Mumbai, India*

<sup>s</sup>*HECR Group, Tata Institute of Fundamental Research, Mumbai, India*

---

## Abstract

We report on the response of a prototype CMS hadron calorimeter module to charged particle beams of pions, muons, and electrons with momenta up to 375 GeV/c. The data were taken at the H2 and H4 beamlines at CERN in 1995 and 1996. The prototype sampling calorimeter used copper absorber plates and scintillator tiles with wavelength shifting fibers for readout. The effects of a magnetic field of up to 3 Tesla on the response of the calorimeter to muons, electrons, and pions are presented, and the effects of an upstream lead tungstate crystal electromagnetic calorimeter on the linearity and energy resolution of the combined calorimetric system to hadrons are evaluated. The results are compared with Monte Carlo simulations and are used to optimize the choice of total absorber depth, sampling frequency, and longitudinal readout segmentation.

PACS Numbers: 29.40.Vj; 29.90.+r; 29.40.Mc; 29.40.Vj Calorimeters 29.90.+r

Other topics in elementary-particle and nuclear physics experimental methods and instrumentation 29.40.Mc Scintillation detectors

Six Keywords: Hadron Sampling Calorimeters, Magnetic Field Effects.

UR-1593, CMS Note 00-003, 6 February 2008

submitted to NIM A

Please send the proofs to: Pawel de Barbaro, U. of Rochester  
c/o Fermilab MS318, P.O. Box 500, Batavia, IL 60510, USA  
tel: 630-840-5639, fax: 630-840-6485, email: barbaro@fnal.gov

---

## 1 The CMS Scintillator Tile-Fiber Hadron Calorimeter

The hadron calorimeter (HCAL) for the Compact Muon Solenoid (CMS) Detector will be used in the determination of quark, gluon, and neutrino final state momenta by measuring the energies and directions of particle jets and the missing transverse energy flow. The determination of the missing energy flow is crucial in searches for new particles and phenomena, such as possible supersymmetric partners of quarks and gluons. Adequate granularity, resolution, and containment of particle showers are essential in attaining these performance goals and provide one of the benchmarks in the design of the CMS hadron calorimeter. In this communication we report on test beam results [1] used in the optimization of the design of HCAL, including choice of total absorber depth, sampling frequency, and longitudinal readout segments.

tation.

The central CMS hadron calorimeter [2,3] is located inside the 4 Tesla coil of the CMS solenoid magnet (inner diameter of 5.9 m). The central pseudo-rapidity range ( $|\eta| < 3.0$ ) is covered by the barrel and endcap calorimeter systems. Segments of the crystal PbWO<sub>4</sub> electromagnetic calorimeter with a silicon pre-shower detector (in the endcap region only) are supported by the barrel and endcap hadron calorimeters. The combined response of the PbWO<sub>4</sub> crystal electromagnetic calorimeter and the hadron calorimeter is used in the reconstruction of particle jets and missing energy in the central pseudorapidity range.

The barrel and endcap sampling hadron calorimeters are located inside the 4 Tesla field of the CMS solenoid. Therefore, the calorimeters are constructed with non-magnetic material. The absorber and structural elements are made out of cartridge brass (70% Cu/ 30% Zn), and stainless steel plates, respectively. Cartridge brass is easy to machine and its hadronic interaction length is approximately 10% shorter than iron. The active sampling elements are 3.7 mm thick plastic scintillator tiles with wavelength-shifting (WLS) fiber readout. The barrel calorimeter inside the solenoid is relatively thin (about 7 interaction lengths at  $\eta = 0$ ). To ensure adequate sampling depth for  $|\eta| < 1.4$ , a hadron outer calorimeter is installed outside the solenoid. The outer calorimeter utilizes the solenoid magnet as an additional absorber equal to  $1.4/\sin(\theta)$  interaction lengths and is used to identify and quantify the contrib-

bution from late starting showers.

### 1.1 Design Requirements

The design of the central hadron calorimeter requires good hermeticity, good transverse granularity, moderate energy resolution, and sufficient depth for hadron shower containment. We have chosen a lateral granularity of  $\Delta\eta \times \Delta\phi = 0.087 \times 0.087$  for  $|\eta| < 2.0$ . This granularity is sufficient to insure good di-jet separation and mass resolution. The calorimeter readout is required to have a dynamic range from 20 MeV to 3 TeV. The sensitivity at the low end allows for the observation of single muons in a calorimeter tower for calibration and trigger redundancy. The scale at the high end is set by the maximum energy expected to be deposited by a jet in a single calorimeter tower.

Initial simulations of the CMS calorimeter indicate that a resolution of  $\sigma_E/E = 120\%/\sqrt{E} \oplus 5\%$  for single incident hadrons is sufficient. In this case, the energy resolution for a jet of particles between 50 GeV and 3 TeV is not degraded by the measurement in the calorimeter, when other fluctuations which are inherent in jets [4] are also considered.

### 1.2 Magnetic Field Effects

Particular attention must be paid to the effects of the high magnetic field on the response of the calorimeter. The intrinsic shower energy development

and the containment of hadron showers have been shown not to be affected by the high magnetic field. However, the scintillator itself exhibits an increased response in a magnetic field. The increased response originates from two sources: (1) an intrinsic brightening of the scintillator ( $\approx 5\%$ ) for B fields above 0.3 Tesla, and (2) a geometric effect due to the increased path lengths of soft electrons in the scintillator. The latter effect depends on the specific orientation of the magnetic field relative to the calorimeter absorber plates.

### *1.3 The Test Beam Program*

A test beam program was initiated in 1994 [5] and was continued in 1995 and 1996. A test module of moveable brass absorber plates and scintillator tile-fiber sampling was exposed to negative hadrons, electrons, and muons in the CERN test beam over a large energy range. During this period the effects of the following sources on the response of the calorimeter module were investigated:

- Magnetic field (scintillator “brightening” and geometric effects)
- Absorber thickness (optimization of resolution versus containment)
- Absorber depth (energy containment)
- Absorber non-uniformity (presence of the magnet coil)
- Crystal electromagnetic calorimeter ( $e/\pi$  effects)

Data were taken both with and without a prototype lead tungstate crystal electromagnetic calorimeter (ECAL) placed upstream of the HCAL module. These data have been used in the optimization of the HCAL design, including the choice of total absorber depth, sampling frequency, and longitudinal readout segmentation.

The test beam data show that the presence of the crystal electromagnetic calorimeter in front of HCAL degrades the linearity and resolution of the combined calorimeter system. However, a large fraction of this degradation can be corrected for by applying constant energy-independent weighting factors to the various longitudinal readout segments of HCAL. The response of the combined calorimeter system using these optimized weights meets the design requirements for resolution and containment of hadron showers.

The experimental setup, various types of studies, and data sets are described in section 2. The measurement of the effects of a magnetic field on the response of HCAL to muons, electrons, and pions is presented in section 3. The performance of HCAL and the combined ECAL+HCAL system is discussed in sections 4 and 5. Extraction of the intrinsic ratio of the response of HCAL to the electromagnetic and hadronic components of the shower,  $e/h$ , is presented in section 6. The optimization studies leading to the choices for the total absorber depth, absorber sampling frequency, and longitudinal readout segmentation is presented in section 7. A comparison of the test beam results with Monte Carlo simulations is discussed in section 8. Section 9 gives a

summary of the results and conclusions.

## 2 Experimental Setup

The combined ECAL+HCAL calorimetric system for CMS has been tested in 1995 and 1996 at the H2 and H4 beamlines at CERN. Data were taken using beams of muons, electrons, and hadrons, ranging in momenta from 15 to 375 GeV/c. These test beam prototypes of HCAL are based on the hanging file [5] structure, in which copper alloy [6] absorber plates ( $\lambda_{INT}(\text{Cu})=15.06$  cm) varying in thickness from 2 cm to 10 cm are interspersed with scintillator tiles read out with WLS fibers [7]. Each scintillator tile is read out independently with a photomultiplier tube (PMT) located at the end of 10 m long optical cable. The total interaction depth of the HCAL prototypes corresponds to  $10.3 \lambda_{INT}$  (H2, 1995 setup),  $8.5 \lambda_{INT}$  (H4, 1995 setup), and  $10.1 \lambda_{INT}$  (H2, 1996 setup). The transverse size of the prototype scintillator tiles is 64 cm  $\times$  64 cm. Details of the H2(1995), H4(1995), and H2(1996) experimental setups are shown in Figure 1. The longitudinal segmentation of each of the modules is described in Tables 1 through 3.

In the H2(1995) run, the HCAL prototypes have been tested with the detector placed inside a large 3 Tesla magnet [8]. The orientation of the magnetic field, with B field lines perpendicular to the scintillator planes (magnetic field parallel to the beam) corresponds to the endcap configuration of a typical

collider detector. The H2(1995) tests include an ECAL module consisting of a lead-scintillator sampling calorimeter, with 10 layers of 1.6 cm Pb interspersed with 6 mm thick scintillator plates. The transverse size of the lead-scintillator sampling ECAL calorimeter for the H2(1995) is 32 cm×32 cm.

During the H4(1995) run, the combined lead tungstate crystal ECAL+HCAL CMS prototype calorimeter has been tested with no magnetic field. The prototype H4(1995) ECAL detector consists of a matrix of  $7\times 7$  PbWO<sub>4</sub> crystals, each 23 cm long ( $25.8 X_0$ ,  $1.1 \lambda_{INT}$ ), and 2 cm×2 cm in transverse dimensions. The total transverse size of the ECAL module matrix is 14 cm×14 cm. The crystal ECAL module is placed approximately 50 cm upstream of the front face of the HCAL prototype. The PbWO<sub>4</sub> crystals are read out by avalanche photodiodes [9] (APD) with a gain approximately equal to 50.

The combined crystal ECAL+HCAL calorimetric system has been tested again in 1996 at the CERN H2 beamline with a magnetic field. The 3 Tesla magnet is oriented in such a way that the lines of the B field are parallel to the scintillator planes, corresponding to the HCAL barrel configuration. For the first 5 interaction lengths of the calorimeter, the magnetic field is uniform to within 10%. Figure 2 shows the relative value of the magnetic field, as a function of depth in HCAL.

## 2.1 The Relative Calibration of HCAL Layers

For the H2(1995) and H4(1995) tests, each scintillator tile is read out by 20 parallel WLS fibers. Figure 3 shows the details of the design of a single scintillator tile. Twenty parallel grooves, spaced every 3.2 cm, are machined with a ball-groove tool bit in 4 mm thick SCSN-81 scintillator plates. The tiles are painted at the edges using Bicron BC-620 white reflective paint, wrapped with white reflective *Tyvek* [10], and sealed for light leaks with a black *Tedlar* [11]. The WLS fibers are mirrored at one end, placed in the grooves, and epoxied in groups of ten into two optical connectors placed at the edge of each scintillator tile, as shown in Figure 3. The stainless steel tubes are installed inside a 2 mm plastic cover and used to guide a radioactive Cs<sup>137</sup> source for calibration purposes. The entire package is held together with a set of brass rivets.

For the H2(1996) tests, a different set of scintillator tiles is used. These tiles are closer to the tower geometry of the final CMS design. Each tile is segmented into a 3×3 matrix read out by nine WLS fibers inserted into  $\sigma$  pattern grooves and is connected to a single PMT. The scintillator tile layout is shown in Figure 4. The tiles are made from 4 mm thick SCSN-81 scintillator produced by Kuraray. Multiclad Y-11 WLS fibers, made by Kuraray, 0.83 mm in diameter, are used. The cross-sectional view of a scintillator tile is shown in Figure 5. Scintillator tiles are packaged between 2 mm thick and 1 mm thick

plastic covers. The transverse uniformity of response of the scintillator plates, measured [12] using a radioactive photon source, has an rms of 4%.

A schematic view of the CERN H2 test beam setup is shown in Figure 6. The calorimeter is placed inside a superconducting magnet, which provides a magnetic field of up to 3 Tesla. Each scintillator tile is read out independently by a 10 stage, EMI 9902 KA photomultiplier tube. Optical cables carry light from the scintillator tiles to the PMT box. In order to avoid large PMT gain variations from the fringe fields of the magnet, the PMTs are located approximately 5 m away from the magnet, behind a 1 m thick iron wall. At this location, the fringe field for the magnet at 3 Tesla is approximately 50 Gauss. Therefore, each PMT can be adequately shielded by a regular inner  $\mu$ -metal shield and an outer, 3 mm thick, soft iron pipe.

The phototube calibration system is a crucial part of the setup. In order to understand the effects of the B field on the phototube gains, several redundant calibration schemes to monitor the PMT gain variation are used. The relative calibration of the scintillator tiles is established with an accuracy of  $\approx 3\%$  by equalizing the average response of each layer to muons. Figure 7 shows an ADC spectrum for 225 GeV/c muons traversing a single scintillator layer. The absolute light yield of each scintillator tile, determined using muons, is approximately 1.5 photoelectrons per minimum ionizing particle. This light yield is sufficiently high such as to not contribute significantly [13] to the hadronic energy resolution of HCAL.

An independent method of monitoring the gain of each tile is provided by a system of radioactive source guide tubes [14]. A radioactive Cs<sup>137</sup> source located at the tip of a long stainless steel wire is periodically inserted into guide tubes embedded in the plastic cover sheet for each tile. The source is moved using a computer controlled source driver.

The muon calibration and the wire source calibration schemes monitor variations in the product of the light yield of the scintillator tiles and the gain of the photomultipliers. In order to separately monitor variations in phototube gains (from temperature dependence and B fringe field effects), each PMT is also connected to a special scintillator block via a set of separate Y11 calibration fibers. The scintillator block is excited using either a laser beam, or a Cs<sup>137</sup> source. In addition, the Y11 calibration fibers can be excited by a light from a blue light emitting diode (LED). The scintillator block is located in a region with a low (approximately 50 Gauss) magnetic field, and thus is in a region where scintillator brightening from the fringe magnetic field is below 1% [15].

### 3 Calorimeter Performance in a Magnetic Field

The CMS hadron calorimeter, which uses plastic scintillators, will operate in a high magnetic field (4 Tesla). As has been previously observed [15–17], the light yield of plastic scintillators placed in high magnetic fields increases by 5 to 8%. This increase is due to polymer excitation that increases the energy of

the short wavelength primary light in the ultra-violet (UV) region.

In addition, the presence of a magnetic field can affect [5,18] the energy deposited in active parts of a sampling calorimeter. To understand this, the response of HCAL to muons, electrons, and pions has been studied as a function of magnetic field strength and orientation for several different sampling configurations. For all magnetic field studies the ECAL module was moved out of the beamline. During the H2(1995) tests, the B-field was oriented perpendicular to the scintillator planes, corresponding to the endcap HCAL configuration, while during the H2(1996) tests, the B-field was parallel to scintillator planes, corresponding to the barrel HCAL configuration.

### *3.1 B field perpendicular to the scintillator planes (endcap configuration)*

When the magnetic field lines are perpendicular to the scintillator planes, the intrinsic light yield of the scintillator is higher than in the case where there is no magnetic field. This scintillator brightening effect leads to the same overall increased response of the calorimeter to muons, electrons, and pions. Figure 8 shows the response of HCAL to pions and electrons as a function of B field relative to B=0 Tesla. The observed  $\approx 5\%$  increase in the response of the calorimeter to particles is consistent with the increased light yield of the scintillator plastic, as measured by the calibration system using the radioactive Cs<sup>137</sup> photon source.

Figure 9 shows a comparison of the average shower profile for 300 GeV/c pions for two magnetic field settings: B=0 Tesla and B= 3 Tesla. The average energy deposition per sampling layer, in minimum ionizing particles (mips), is plotted as a function of HCAL absorber depth. Since the gain of each scintillator layer is established by equalizing its response to muons independently for the 0 T and 3 T data sets, the effect of scintillator brightening is already removed. As can be seen in the figure, the shape of the pion shower profiles remains unchanged in the presence of a 3 Tesla magnetic field perpendicular to the scintillator planes.

In summary, we conclude that a B field perpendicular to the scintillator planes results in an overall increase in the scintillator light yield. This scintillator brightening effect can be effectively measured by the calibration system using a radioactive  $\gamma$  source.

### *3.2 B field parallel to the scintillator planes (barrel configuration)*

In contrast, when the magnetic field lines are parallel to the scintillator planes, the observed average hadron shower profiles are altered. A comparison of the average observed shower profiles for 300/c GeV pions as a function of the HCAL absorber depth, for B = 0 and B = 3 Tesla, is shown in Figure 10. Energy deposited by hadron showers in mips shows an additional increased response, in the B = 3 Tesla field, relative to the B= 0 Tesla case.

The relative average response of HCAL to 100 GeV/c electrons and pions as a function of magnetic field is shown in Figure 11. As indicated by the data, the HCAL response to electrons in mips increases by approximately 20% at B=3 Tesla, relative to B=0 Tesla. However, the response for pions in mips increases by only  $\approx$  8%. The results are compared to simulations using the GEANT [19] Monte Carlo program (10 GeV/c electrons and 50 GeV/c pions). As shown in the figure, the simulations reproduce data well.

Studies using a GEANT Monte Carlo simulation indicate that the increased response is due to a geometric effect resulting from a change in the path length of low energy electrons (between 1 and 10 MeV) exiting the absorber plates and traversing a circular path in the scintillator layer (because of the strong magnetic field). The radius of curvature of a 1 MeV/c electron in a 3 Tesla magnetic field is approximately 1 mm. The size of this geometric effect is expected to be proportional to the strength of the B field and depends on the detailed structure [18] and composition of the absorber/scintillator package.

A GEANT study models the calorimeter response to 10 GeV electrons as a function of the air gap between the scintillator package and the upstream absorber (see Figure 12) in the presence of a strong magnetic field. The results are summarized in Figure 13. The increase in the electron response is reduced as the distance between scintillator package and upstream absorber is increased.

The results presented so far have been taken with the scintillator package placed in the absorber gap in the following way: 1 mm plastic + 4 mm scintillator + 2 mm plastic, with respect to the beam direction. In this configuration (configuration A), the scintillator is separated from the upstream-most absorber plate by  $1 \text{ mm} \pm 0.5 \text{ mm}$  of air and 1 mm of plastic. The Monte Carlo studies indicated that the effect of a parallel magnetic field depends on the distance between the scintillator and the most upstream absorber. Therefore, we have investigated the calorimeter response to pions, electrons, and muons with the reversed orientation of the scintillator package in the absorber gap (configuration B). In configuration B, the position of the scintillator package relative to the beam direction is: 2 mm plastic + 4 mm scintillator + 1 mm plastic. In the case of configuration B, the scintillator is separated from the upstream most absorber plate by  $1 \text{ mm} \pm 0.5 \text{ mm}$  of air and 2 mm of plastic.

Figure 14 shows the average electron and pion response of HCAL in mips as a function of B field, relative to the response at  $B= 0$  Tesla, measured with the configuration B scintillator package. Here, we measure the response of electrons at  $B = 3$  Tesla to be only  $14 \pm 1\%$  higher (relative to  $B = 0$  Tesla), compared to  $20\% \pm 1\%$  effect for configuration A. GEANT simulation reproduces the electron data well. The additional 1 mm plastic upstream of the scintillator in configuration B (vs configuration A) helps range out more low energy electrons coming out of the upstream absorber plate.

In order to minimize the effect of the magnetic field on the response of the CMS

hadron barrel calorimeter, one would like to maximize the distance between the scintillator and the upstream absorber. Therefore the configuration B of scintillator placement in the gaps between absorber plates has been chosen for the CMS HCAL design. A system of thin brass (Venetian Blind type) springs pushes the scintillator tiles radially outwards, such that the scintillator is always positioned closest to the downstream absorber plate. The use of springs ensures that the distance between inner absorber and the scintillator plate will consist of  $2 \text{ mm} \pm 0.5 \text{ mm}$  of air and  $2 \text{ mm}$  of plastic.

Figure 15 shows the ratio of HCAL response to pions as a function of pion energy, at 3 Tesla and 1.5 Tesla, relative to its response at 0 Tesla for the two configurations of the scintillator package inside the absorber gap. The lines shown on the Figure 15 indicate the values for  $\pi(3T)/\pi(0T)$  and  $\pi(1.5T)/\pi(0T)$  as a function of particle momentum. These functions were calculated using the Wigmans [21] and Groom [25] parameterizations<sup>1</sup> of the average fraction of the electromagnetic component in pion showers. The average fraction of the electromagnetic component in pion showers increases as a function of pion energy. With  $e/h$  of HCAL greater than unity, this increase results in non-linearity of HCAL response to pions. For example, the relative response of the calorimeter to 300 GeV/c pions is higher by  $\approx 5\%$ , with respect to 50 GeV/c pions. However, a 3 Tesla magnetic field increases the  $e/h$  ratio for HCAL by

---

<sup>1</sup> Detailed study of the average fraction of the electromagnetic component in pion showers,  $F(\pi_0)$ , and extraction of  $e/h$  is presented in section 6.

$\approx 20\%$  for configuration A and 14% for configuration B, see Figs. 11 and 14.

Therefore, a 3 Tesla magnetic field is expected to increase the non-linearity of HCAL's response to pions between 50 GeV/c and 300 GeV/c by an additional  $\approx 2\text{-}3\%$ .

The above estimate is relevant only for the subset of single pions which interact in HCAL (minimum ionizing in ECAL). However, in the actual CMS detector, the common situation is that of a jet of particles depositing a large fraction of energy in the ECAL calorimeter. Since the ECAL calorimeter is not sensitive to magnetic field effects, the additional non-linearity from the 3 Tesla B field is greatly reduced.

In summary, a B field parallel to the scintillator planes results in an increased response due to two effects: (a) the scintillator brightening effect and (b) an additional increase in the response to the electromagnetic component of hadron showers (geometrical effect). The latter effect is strongly dependent on the placement of the scintillator packages with respect to the absorber plates of the calorimeter.

The results reported in this paper are consistent with earlier reports on the behavior of plastic scintillators in magnetic fields [15,17] and on the influence of magnetic fields on response of scintillator based calorimeter [16]. Note however, that in the latter publication the conclusion that electron response follows the dependence of the light yield ("brightening effect") is true only for

magnetic fields below 0.3 Tesla. As shown in this report, in the presence of parallel magnetic fields above 0.3 Tesla, the geometric effect leads to additional increase in response of the sampling calorimeters to electrons.

We also note that the origin of the latter effect is due to the relative geometry of the absorber with respect to the active elements of the calorimeter and is not sensitive to any special property of the scintillator as the active sampling medium. Therefore, similar effects are expected for any type of sampling calorimeters, with similar magnetic field/absorber configurations, independent of the choice of material for the active sampling medium.

#### **4 Performance the HCAL calorimeter with a Pb-Scintillator ECAL**

During the H2(1995) running period, a Pb-scintillator ECAL calorimeter was placed in front of the HCAL calorimeter. Linearity of the response and energy resolution of the combined system was studied for electrons, pions, and muons with momenta from 50 to 300 GeV/c.

In the following discussion we consider two different samples of pion data. The first, which we refer to as "mip-in-ECAL" pions, includes only pions which are minimum ionizing in ECAL, i.e. do not interact in ECAL and begin interacting in HCAL. This sample is selected by requiring that the energy deposition in ECAL is consistent with minimum ionizing deposition, i.e. is less than 2.5 GeV. The second sample, which we refer to as the "full pion sample", includes

all pions, i.e. interacting in either ECAL or HCAL.

The absolute energy scale of the HCAL calorimeter is set using 300 GeV/c "mip-in-ECAL" pions. The average pulse height deposited by muons in HCAL corresponds to approximately 3 GeV of equivalent hadronic energy. Figure 16 shows the energy deposited by 225 GeV/c muons in HCAL. A pedestal trigger is a random trigger during the beam. This pedestal distribution is shown as a dashed line in Fig. 16. The width of the energy distribution for random pedestal triggers is equivalent to 80 MeV. Hence, the contribution of electronic noise to the energy resolution of HCAL is negligible.

The absolute energy scale of the ECAL calorimeter is set using 50 GeV/c electrons. The energy response of the Pb-scintillator sampling ECAL calorimeter ( $\approx 2.9 X_0$  sampling) for electrons with momenta in range 50 to 150 GeV/c is linear to within 1%. The fractional energy resolution for 50 and 100 GeV/c electrons is 7.2% and 6.2%, respectively.

The energy response of the combined Pb-scintillator ECAL+HCAL calorimeter system is calculated as follows:

$$E_{TOT} = \sum_i^{ECAL} \frac{ADC_i * w_i}{\mu_i} / Escale + \sum_j^{HCAL} \frac{ADC_j * w_j}{\mu_j} / Hscale \quad (1)$$

Here,  $Escale$  and  $Hscale$  are constants which define the absolute energy scales of ECAL and HCAL, and  $ADC_i$  are the ADC values of each readout layer of ECAL and HCAL. The relative calibration constants of each layer,  $\mu_i$ ,

correspond to the average muon response of a layer expressed in units of ADC counts. The coefficients  $w_i$  are proportional to the arithmetic mean of the interaction lengths of the absorber plates upstream and downstream of each scintillator layer (the "Simpson" approximation formula),  $w = 0.5 \times (t_{upstream} + t_{downstream})$ .

Scatter plots of the energies in HCAL vs ECAL for 50, 100, 150, and 300 GeV/c particles in the hadron beam are shown in Figure 17. As indicated in the figure, the nominal hadron beam, especially at the 50 GeV/c and 100 GeV/c beam tunes, contains a large fraction of electrons. Pion induced events are selected by requiring that energy deposited in HCAL is at least 0.5 GeV. In order to remove particles that interact upstream of ECAL, the energy deposition in the first ECAL layer is required to be consistent with that of a minimum ionizing particle.

The total (ECAL+HCAL) energy distributions for "mip-in-ECAL" pions are shown in Figure 18. The total energy distributions for the "full pion sample" are shown in Figure 19. The reconstructed energy distributions are well described by Gaussian fits for both sets of data. Figure 20 shows the linearity versus energy for the calorimeter response for "mip-in-ECAL" pions, and for the "full pion sample" using the Pb-scintillator ECAL+HCAL calorimetric system. The average response of the combined Pb-scintillator ECAL+HCAL system to the "full pion sample" is approximately 1% lower than the response of the calorimeter for the subset of "mip-in-ECAL" pions.

A comparison of the relative energy resolutions of the calorimeter for "mip-in-ECAL" pions and for the "full pion sample" is shown in Figure 21. The energy resolutions for these two cases are comparable. At low energies, the energy resolution of the "full pion sample" is slightly improved because of the finer sampling of the Pb-scintillator ECAL.

The fractional energy resolutions are parameterized by the following function:

$$\sigma_E/E = (\text{stoch. term})/\sqrt{E} \oplus (\text{const. term}) \quad (2)$$

Here  $E$  is the particle energy in GeV, and the symbol  $\oplus$  implies that the stochastic and constant terms in the resolution are combined in quadrature.

The following values for the stochastic term and the constant term are extracted from the data:

$$\sigma_E^{\text{pions mip in ECAL}}/E = (93.8 \pm 0.9)\%/\sqrt{E} \oplus (4.4 \pm 0.1)\% \quad (3)$$

for "mip-in-ECAL" pions, and

$$\sigma_E^{\text{all pions}}/E = (82.6 \pm 0.6)\%/\sqrt{E} \oplus (4.5 \pm 0.1)\% \quad (4)$$

for the "full pion sample".

## 5 Performance of the HCAL calorimeter with a PbWO<sub>4</sub> crystal ECAL

In this section the linearity of response and energy resolution of the HCAL calorimeter with a PbWO<sub>4</sub> crystal matrix ECAL are discussed. The performance of the combined PbWO<sub>4</sub> ECAL+HCAL calorimetric system was first investigated during 1995 in the H4 beamline.

The calibration of the ECAL crystals uses 50 GeV/c electrons directed into the center of each crystal. Figure 22 shows the energy response of ECAL for 25, 50, 100, and 150 GeV/c electrons using the  $7 \times 7$  ECAL matrix sum. The energy resolutions of the crystal ECAL at these energies are found to be 0.6 GeV, 0.7 GeV, 1.0 GeV, and 1.4 GeV, corresponding to fractional energy resolutions of 2.4%, 1.4%, 1.0%, and 0.9%, respectively. During these tests, the electronic noise of the  $7 \times 7$  crystal matrix energy sum had a rms width equivalent to 440 MeV. Much better performance of the crystal ECAL calorimeter has been attained [20] in other tests which were dedicated to special ECAL studies.

The energy response of the combined crystal ECAL+HCAL calorimeter system is calculated as follows:

$$E_{TOT} = \sum_i^{ECAL} \frac{ADC_i}{e_i} / Escale + \sum_j^{HCAL} \frac{ADC_j * w_j}{\mu_j} / Hscale \quad (5)$$

Here, *Escale* and *Hscale* are constants which define the absolute energy scales of ECAL and HCAL,  $ADC_i$  are the ADC values of each readout layer (tower)

of the HCAL (ECAL) calorimeter. The relative calibration constants of each tower of ECAL,  $e_i$ , correspond to the average 50 GeV/c electron response of a tower expressed in units of ADC counts. The coefficients  $w_j$  and  $\mu_j$  are defined as before (Eqn. 1).

Figure 23 shows a scatter plot of the energy deposition in HCAL versus ECAL taken during the H4(1995) test beam run with pions with momenta ranging between 15 and 375 GeV/c. Unlike in the case with the Pb-scintillator ECAL, the data points are not centered on a straight line corresponding to  $E_{ECAL} + E_{HCAL} = p_{beam}$ . The energy response of the HCAL calorimeter to "mip-in-ECAL" pions is shown in Figure 24. The response of the combined crystal ECAL+HCAL calorimeter to the "full pion sample" is shown in Figure 25. The distributions for the combined crystal ECAL+HCAL system deviate from a Gaussian shape, especially at low energies.

As demonstrated earlier, the H2(1995) data with a Pb-scintillator ECAL show good linearity for the combined ECAL+HCAL calorimeter system. However, as can be seen in Figure 26, the H4(1995) data with a  $PbWO_4$  crystal ECAL is quite non-linear. In addition, the average response of the combined crystal ECAL+HCAL calorimeter to "full pion sample" is approximately 10% lower than the response to pions which interact in HCAL only.

Figure 27 shows the fractional energy resolutions of the calorimeter for the "mip-in-ECAL" pions for the "full pion sample". The energy resolutions of

the combined crystal ECAL+HCAL calorimeter system are significantly degraded, especially at high energies. These results are attributed to the large difference between the response of the crystal ECAL to electrons and hadrons, i.e. the large  $e/h$  (the ratio of the response to the electromagnetic and hadronic components of the shower) of the PbWO<sub>4</sub> crystals. This large  $e/h$  results in an overall response of the calorimeter which is very sensitive to fluctuations in the initial electromagnetic component of hadronic showers.

A fit to data for the fractional energy resolution yields the following values for the stochastic term and constant term parameters:

$$\sigma_E^{pions \text{ } mip \text{ } in \text{ } ECAL}/E = (101 \pm 0.1)\%/\sqrt{E} \oplus (4.0 \pm 0.1)\% \quad (6)$$

for the case of "mip-in-ECAL" pions , and

$$\sigma_E^{all \text{ } pions}/E = (127 \pm 0.7)\%/\sqrt{E} \oplus (6.5 \pm 0.1)\% \quad (7)$$

for the case of the "full pion sample". Note that the first fit ("mip-in-ECAL" data , eqn. 6) is consistent with the H2(1995) "mip-in-ECAL" data (eqn. 3).

## 6 Response of HCAL to electrons and the $e/h$ ratio for HCAL

The linearity and energy resolution of hadron calorimeter depends [21] on the intrinsic  $e/h$ . The average fraction of the energy in the electromagnetic component of hadron induced showers,  $F(\pi^0)$ , increases as a function of in-

cident energy. For non-compensating calorimeters ( $e/h \neq 1$ ), this implies a non-linear hadron energy response. The event-by-event fluctuations in  $F(\pi^0)$  contribute to variations in the reconstructed shower energy and dominate the energy resolution for hadrons at high energies.

In order to study the relative response of HCAL to electron and pions, data were taken with ECAL removed from the beamline. In order to reject electrons present in the hadron tunes from the sample, a minimum ionizing signal was required in the first three sampling layers of HCAL.

The studies of the energy response of HCAL to pions indicate that the HCAL calorimeter is somewhat non-linear. There is  $\approx 9\%$  increase in the relative response of HCAL to pions between 15 and 375 GeV/c, as shown in Figure 28. The total interaction length <sup>2</sup> of the H4(1995) HCAL module is approximately  $8 \lambda_{INT}$ . At very high energies, an  $8 \lambda_{INT}$  calorimeter is not expected to fully contain the hadronic shower. The correction for longitudinal leakage for an  $8 \lambda_{INT}$  calorimeter is estimated [22] to be 1.5% at 120 GeV/c and 3.5% at 375 GeV/c, using CCFR [23] and NuTeV [24] test beam data. Therefore, the intrinsic non-linearity of HCAL is somewhat larger if the corrections for leakage at high energies are applied.

The response of the H4(1995) HCAL module to electrons is linear at a level

---

<sup>2</sup> Taking into account the requirement that energy deposition in first three HCAL counters is consistent with minimum ionizing particles.

of 2% and is approximately 15% higher than the average response to pions as shown in Figure 28. The absolute energy scale of HCAL is set (as before) by the 375 GeV/c pion data point.

The electron and pion data can be used to extract  $e/h$  by applying the following expressions:

$$\pi = F(\pi^0) \times e + (1 - F(\pi^0)) \times h \quad (8)$$

$$\frac{\pi}{e} = \frac{1 + (\frac{e}{h} - 1) \times F(\pi^0)}{\frac{e}{h}} \quad (9)$$

Here  $e$  is the response of the calorimeter to the electromagnetic components of hadron showers and  $h$  is the response to the hadronic component of pion showers.  $\pi$  is the response to pions and  $F(\pi^0)$  is the fraction of the energy in electromagnetic component of pion showers.

The extracted value of  $e/h$  depends on the assumed parameterization for  $F(\pi^0)$  as a function of energy. The Wigmans [21] formula for  $F(\pi^0)$  (eqn. 10) increases with energy ( $\approx \log(E)$ ) and becomes non-physical at very high energies. The Groom parameterization (eqn. 11) is extracted from a CALOR Monte Carlo simulation [25] and uses a power law dependence.

$$F_W(\pi^0) = 0.11 \times \ln(E) \quad (10)$$

$$F_G(\pi^0) = 1 - (E/0.96)^{0.816-1} \quad (11)$$

Using the above two parameterizations, we extract values of  $e/h$  of  $1.41 \pm$

0.01 (Wigmans) and  $1.51 \pm 0.01$  (Groom). The best fit to our data is shown in Figure 29.

The above results can be compared with similar analyses for other iron-scintillator sampling calorimeters. Extraction of  $e/h$  for an iron-scintillator sampling calorimeter has also been done [26] by CDF. The CDF endcap hadron calorimeter consists of 22 layers of 5 cm iron absorber plates and 6 mm scintillators. The CDF results yield  $e/h = 1.34 \pm 0.01$  (Wigmans) and  $1.42 \pm 0.015$  (Groom). ATLAS [27] measures  $e/h = 1.34 \pm 0.03$  assuming the Wigmans parameterization for  $F(\pi^0)$ . The ATLAS hadron calorimeter uses iron as an absorber with the tiles are oriented in the radial direction.

The NuTeV Collaboration reports a  $e/h$  ratio for 10 cm iron sampling calorimeter [24] of  $1.08 \pm 0.01$  using the Groom parameterization. Note that  $e/h$  is sensitive to the sampling fraction and other geometrical effects. The CCFR/NuTeV calorimeter uses 2.5 cm thick liquid scintillator counters, which are clad with acrylic and water bags. The cladding and the thick scintillators in CCFR/NuTeV greatly reduce the response to electrons relative to the response to pions. Also, the water and thick scintillators tend to increases the rate of conversion of low energy neutrons to protons in the active medium.

## 7 Optimization of the design of HCAL

The conceptual design of the barrel HCAL was a  $5.3 \lambda_{INT}$  thick calorimeter. The inner half of the calorimeter had 3 cm sampling (first readout segment, H1) while the second readout segment consisted of the outer half of the calorimeter with 6 cm sampling.

For the H2(1996) tests, the prototype HCAL module was segmented into 27 readout layers. Using these data we simulated various sampling configurations and studied the performance of HCAL as a function of total interaction length and sampling frequency. These data allowed us to optimize the calorimeter response to pions and jets, while taking into account the existing design (e.g. geometrical and readout) constraints imposed on HCAL within the CMS detector.

Important design choices that were made based on these data are:

- the absorber sampling thickness;
- the depth of the HCAL inside the magnet (in interaction lengths);
- the longitudinal segmentation of the inner HCAL into H1 and H2 readout segments;
- possibility of adding scintillator layers outside of the magnet to create an outer calorimeter.

### *7.1 Choice of the longitudinal segmentation for HCAL*

Studies performed prior to the H2(1996) beam tests resulted in no compelling argument to set the optimal partition between the two readout segments of inner HCAL. However, the 1996 test beam data indicate that the proper partition is that which is most useful in correcting for large  $e/h$  response of the ECAL crystals. To compensate for a large  $e/h$  of the combined ECAL + HCAL system, we chose to make a novel longitudinal segmentation, with the first depth segment, H1, reading out only the first scintillator layer. The remaining scintillator layers inside the magnet are combined into the second readout, H2. The reason for this choice is the following. A large H1 signal indicates that a significant amount of hadronic energy has been deposited in ECAL and is underestimated because of the large  $e/h$  of the crystals. The information from H1 can be used to make an effective correction for the hadronic non-linearity of the ECAL crystals.

### *7.2 Response of the combined crystal ECAL+HCAL calorimeters*

Figure 31 and 32 show the energy response and fractional energy resolutions of the combined PbWO<sub>4</sub> crystal ECAL+HCAL calorimeters to pions. The inner HCAL( $5.3 \lambda_{INT}$ ) consists of two independent readouts: H1 (following a 2 cm Cu plate) and H2 (thirteen 6 cm Cu samplings). A single readout outer calorimeter (HO) consists of three samplings: (1) the first sample is

immediately after the magnetic coil (which is mimicked by 18 cm of Cu in the test beam ),(2) a second 22 cm Cu sampling layer, and (3) a third 16 cm Cu sampling layer. The combined coil and HO samplings correspond to a total of  $2.5\lambda_{INT}$ .

We have investigated two possible approaches to correct for the degradation of the performance of the combined crystal ECAL+HCAL calorimeters. Both of these methods make use of the segmented readout of HCAL. The first approach, called passive weighting, increases the weight ( $\alpha$ ) of the first (H1) HCAL readout segment, where  $\alpha$  is an energy independent constant. Note that  $\alpha = 1$  corresponds to using the standard "absorber Simpson's weighting" used elsewhere in the calorimeter.

$$E_{TOT} = E_{ECAL} + \alpha \times E_{H1} + E_{H2} + E_{HO} \quad (12)$$

The overall linearity and fractional energy resolution of the combined crystal ECAL+HCAL system for 300 GeV/c pions as a function of the parameter  $\alpha$  are shown in Figure 30. Both the linearity and energy resolution of the combined crystal ECAL+HCAL system are improved for the value of  $\alpha = 1.4$ .

The second approach, called dynamic weighting is an event-by-event correction. It depends on the fraction of the energy deposited in the first readout segment of HCAL immediately downstream of the crystal ECAL. The dynamic weighting effectively allows one to have an energy dependent correction

(for single particles) for the low response to pions which interact in ECAL.

$$E_{TOT} = (1 + 2 \times f(H1)) \times E_{ECAL} + E_{H1} + E_{H2} + E_{HO}, \quad (13)$$

$$f(H1) = E(H1)/(E(H1) + E(H2) + E(HO)), \quad f(H1) \leq 0.1 \quad (14)$$

With either the passive or dynamic weighting, the nonlinearity and resolutions for pions with energies between 30 and 300 GeV/c are improved. With the passive weighing, the fractional energy resolution of the combined ECAL+HCAL calorimetric system can be described by the function  $\sigma_E/E = 122\%/\sqrt{E} \oplus 5\%$ . Note that while the passive weighting can be applied to single particles and jets, the dynamic weighting may introduce high energy tails in the case of particle jets.

Techniques to overcome the problem of the different non-compensation properties (i.e.  $e/h$ ) of the electromagnetic and hadronic compartments for combined calorimetry systems have been studied [28] by the ATLAS calorimetry group. The algorithms proposed by the ATLAS group depend on the energy fraction deposited in the electromagnetic compartment and therefore can be only applied to single particle energy reconstruction.

### 7.3 Studies of the total HCAL absorber depth

We use the 27 sampling layers of the H2(1996) test beam module to study the calorimeter performance as a function of total depth. Figure 33 shows the

average pion shower profiles as a function of total absorber depth for 50, 100, 150, and 300 GeV/c pions. As shown in the figure, the average pion shower profiles extend significantly beyond  $7 \lambda_{INT}$ , in particular at high pion energies. Fluctuations in the leakage for high energy pions also become large.

To collect this leakage energy, the barrel HCAL has been augmented with an additional outer calorimeter (HO) consisting of a single layer of scintillators beyond the solenoid magnet (the solenoid thickness is  $1.4 \lambda_{INT}$ ). For pseudo-rapidity  $\eta$  less than 0.4, a layer of iron (thickness = 18 cm =  $1.1 \lambda_{INT}$ ) has been instrumented with an additional scintillator layer. For either case (one or two layers of scintillator), the scintillators cover the same solid angle as the interior calorimeter and are read out as a single depth segment. The combined solenoid + iron of the HO corresponds to an additional  $2.5 \lambda_{INT}$ .

The fraction of 300 GeV/c pions with reconstructed energy less than 200 GeV (approximately  $3\sigma$  below the mean, or 100 GeV of missing energy) is shown in Figure 34. The four points correspond to:  $5.9 \lambda_{INT}$ , the HCAL alone;  $7.0 \lambda_{INT}$ , HCAL + ECAL;  $9.5 \lambda_{INT}$ , HCAL + ECAL + HO; and  $11 \lambda_{INT}$  which is the total thickness of the 27 layer test beam module. We see that for the CMS barrel design, at  $9.5 \lambda_{INT}$ , less than 2% of the pions are catastrophically mismeasured. To increase the interaction length of the calorimeter to  $9.5 \lambda_{INT}$  we added two additional absorber plates inside the magnet with respect to the conceptual design. This was achieved by reducing the inner radius of barrel HCAL.

#### *7.4 Optimization of Absorber Sampling Thickness*

The fractional energy resolution has been investigated for the following three choices for the inner HCAL absorber samplings: a) 3 cm Cu sampling for the first eight layers followed by 6 cm Cu sampling, b) 6 cm Cu uniform sampling, and c) 12 cm Cu uniform sampling. The data, shown in Figure 35 indicate that the energy resolution is not dominated by the sampling fluctuations in HCAL. A factor of two decrease in the sampling frequency ( 3 cm/6 cm to 6 cm uniform sampling) for HCAL does not result in a noticeable degradation of the energy resolution of the combined detector system. In the case of 12 cm Cu uniform sampling, the degradation in energy resolution is noticeable, but does not scale with  $\sqrt{t}$ , where  $t$  is the thickness of the absorber plates. For the final design, we chose uniform 5 cm sampling which does not degrade the energy resolution and puts more absorber inside the magnet, relative to the conceptual design.

#### *7.5 Final Design of CMS Barrel HCAL*

The final design of the CMS barrel HCAL consists of 17 absorber/scintillator samples with 5 cm absorber thickness. The total thickness of absorber at 90 degrees is  $5.9 \lambda_{INT}$ . With the ECAL included, the total thickness inside the magnet is  $7.0 \lambda_{INT}$ . Exterior to the magnet, there is a  $2.5 \lambda_{INT}$  outer calorimeter. Each projective tower has 3 readouts in depth: the very first

scintillator layer (H1); the remaining 16 scintillator layers inside the magnet (H2); and the outer calorimeter (HO).

## 8 Monte Carlo simulation of the test beam results

Several hadron shower generators are available within the GEANT [19] framework. These include GHEISHA [29], GFLUKA (which is an implementation of FLUKA [30] within GEANT), and GCALOR (which is an implementation of CALOR [31] within GEANT). Although GHEISHA is native to the GEANT program, GFLUKA and GCALOR are imperfect implementations of the original FLUKA and CALOR programs. Both of these programs have been known to produce somewhat different results [32] than the original generators.

GEANT is used in various studies for evaluation of the calorimeter design for CMS. In order to verify those simulations and to understand their limitations, GCALOR is used to simulate the H2(1996) test beam data. It also serves as a reference for comparison with the other generators. Our aim is first to anchor the Monte Carlo model to the ensemble of test beam data. Once it is so constrained, it is assumed that it can be used to make small extrapolations to model the final CMS calorimeter system.

Details of the crystal ECAL and HCAL test beam geometry are implemented in the GCALOR simulation. For ECAL, this includes a 7 x 7 matrix of individual crystals surrounded by copper blocks as well as mechanical and cooling

structures. The HCAL geometry includes the layer structure of copper plates, scintillator, plastic cover plates, and air gaps on both sides of each scintillator. In order to take into account all experimental effects, the transverse beam profiles are simulated using information from the test beam tracking chamber. Electronic noise and photo-statistics effects are simulated based on the measured distributions of pedestals, electron, and muon signals in ECAL and HCAL. The longitudinal light collection efficiencies in the central nine crystals are included in the simulation. The energy cut values in the GEANT simulation are set to the GEANT default values, 1 MeV for electrons and 10 MeV for hadrons.

In order to compare response of pions interacting in HCAL, we have removed ECAL from the beam. For this dataset, the test beam data are in good agreement with the results of the GCALOR Monte Carlo simulations. Good agreement is observed in the longitudinal shower profile (Fig. 36), the pion response versus energy (Fig.37), and in the fractional pion energy resolution (Fig.38).

A comparison of the linearity and fractional energy resolutions for the "full pion sample" using the combined crystal ECAL+HCAL system for test beam data and the GEANT simulations are shown Figures 39 and 40. The GEANT simulations, which include all experimental detector effects such as electronics noise, are in good agreement with the test beam data. Also shown in Figure 40 are the results of a MC simulation of the crystal ECAL+HCAL energy resolution excluding test beam detector effects, such as the ECAL electronic noise,

and the energy leakage from the small prototype ECAL. As can be seen in Figures 40, the detector effects present during the H2(1996) test beam data taking significantly degrade the fractional pion energy resolution, especially at the low energies. These test beam detector effects are not expected to be present in the final CMS configuration.

Comparisons of the fractional energy resolution simulated by GCALOR and other GEANT hadron simulators are shown in Figure 41. The simulations based on GHEISHA predict somewhat worse resolutions, while simulations based on GFLUKA+MICAP predict much better resolutions than predicted with GCALOR and observed in the data.

## 9 Conclusions

Comprehensive tests of the performance of prototype CMS central hadron calorimeters have been done in the H2 and H4 beamlines at CERN. Data were taken with both a stand-alone HCAL calorimeter and with HCAL in combination with an upstream ECAL calorimeter.

One of the primary objectives of the HCAL test beam studies was to investigate the calorimeter performance in the presence of perpendicular and parallel magnetic fields. A high magnetic field changes the response of the calorimeter in two different ways: (1) the overall light yield of the scintillator is increased in a high magnetic field and (2) the field affects the observed energy deposition

of electromagnetic components of showers when it is parallel to the scintillator plates (i.e. perpendicular to the particle direction). For a collider experiment with a solenoid magnet, the magnetic field is parallel to the calorimeter plates in the central part of the detector (barrel configuration) and is perpendicular to calorimeter plates in the large  $\eta$  region ( endcap configuration).

When the magnetic field is perpendicular to the scintillator planes (endcap configuration), only an intrinsic increase of the light yield of the scintillator of approximately 5-8% is observed relative to the case with no magnetic field. This effect leads to the same overall increased response of the calorimeter to muons, electrons, pions, and  $\gamma$  rays from a radioactive source. Therefore a calibration source can be used to track and correct for this effect.

An additional geometric effect leads to an increased response of the calorimeter to the electromagnetic component of showers. This effect occurs in the case in which the magnetic field lines are parallel to the scintillator planes (barrel configuration) and originates from an increase in the geometrical path length of low energy electrons in a magnetic field. Since this effect is not present for the calibration source, *in situ* (B field on) calibration is required for hadron barrel calorimeter.

The size of this effect is approximately proportional to the strength of the B field and depends on the detailed structure and composition of the absorber and scintillator planes. However, the effect is expected to be present in any

sampling calorimeter (independent of readout technology) situated in a magnetic field which is parallel to the readout planes (barrel configuration).

Due to the non-compensating nature of the lead tungstate crystal ECAL the linearity and energy resolution of the combined crystal ECAL+HCAL is worse than for HCAL alone. Therefore, improvements in the linearity and resolution using weighting of the two longitudinal readouts (H1 and H2) of HCAL have been investigated. Using a passive weighting, the fractional energy resolution of the combined crystal ECAL+HCAL calorimetric system is described by the function  $\sigma_E/E=122\%/\sqrt{E} \oplus 5\%$ . This performance is achieved by a novel longitudinal segmentation of HCAL with H1 being a single layer immediately behind ECAL. We conclude that for combined ECAL+HCAL calorimeter systems with an ECAL with a large e/h, a very thin first depth segment in HCAL can be used to largely correct for the resultant non-linearity and degradation in energy resolution. Monte Carlo studies of the CMS detector in a collider environment indicate that with the above performance, the energy resolution for jets is not dominated by the energy measurement in the hadron calorimeter, but by other fluctuations which are inherent in jets [4].

We find that the average longitudinal hadron shower profiles extend past the inner HCAL located inside the magnetic coil. Therefore, the CMS central calorimeter design includes instrumenting an outer calorimeter (HO) outside the coil to measure the energy in the tail of high energy hadronic showers. The addition of HO leads to a total ECAL+HCAL+HO depth of at least 9.5

$\lambda_{INT}$  for almost the entire  $\eta$  range spanned by the CMS hadron calorimeters.

Various GEANT based simulations predict the impact of the performance of HCAL on a variety of potential physics searches in the CMS detector. These simulations extrapolate the performance of HCAL from the test beam configuration to the final configuration chosen for CMS HCAL design. The Monte Carlo programs have been shown to successfully simulate various test beam setups, including hadron shower calorimetry in a setting with both crystal and copper-scintillator detectors in a strong magnetic field. The best description of the data is provided by GEANT with the GCALOR module for the generation of hadron showers.

## 10 Acknowledgments

We thank the CERN staff and the staff of the participating institutions for their vital contributions to this experiment. We particularly acknowledge efforts of Maurice Haguenauer and Jean Bourrette (H4 beamline), Pascal Petiot, and Gerhard Waurick (H2 beamline), Brian Powell (3T magnet), Albert Ito (PMTs), as well as Anatoly Zarubin (DAQ).

## References

- [1] The contact person for further details on these test beam studies is Pawel de Barbaro, University of Rochester, (barbaro@fnal.gov).
- [2] The Compact Muon Solenoid (CMS) Technical Proposal, CERN/LHCC 94-38, December 15, 1994.
- [3] CMS Hadron Calorimeter Technical Design Report, CERN/LHCC 97-31, June 20, 1997.
- [4] CMS Response Document to LHCC Referees, Appendix A1 to CMS HCAL TDR, CERN/LHCC 97-31.
- [5] V. Abramov *et al.*, *Study of Magnetic Field Influence on Hadron Calorimeter Response*, IHEP preprint 96-91.
- [6] The absorber plates are composed of copper alloy (brass) with the following composition: 59% Cu, 39% Zn, 1% Fe, 1% Mn.
- [7] *Scintillator Tile-Fiber Calorimeters for High Energy Physics: The CDF End Plug Upgrade, Selected Articles.*, edited by P. de Barbaro and A. Bodek, University of Rochester preprint UR-1309, October 1994.
- [8] M. Aguilar-Benitez *et al.*, *Nucl. Instrum. Methods A***258** (1987) 26; *Status report of the RD5 experiment*, CERN-DRDC/93-49.
- [9] CMS Electromagnetic Calorimeter Project Technical Design Report, CERN/LHCC 97-33, CMS TDR 4, 15 December, 1997.
- [10] Tyvek B1060 (registered trademark of DuPont Co.) is a thin sheet of high density white polyethylene.

- [11] Tedlar TCC15BL3 (registered trademark of DuPont Co.) is a black opaque film of polyvinyl fluoride polymer.
- [12] P. de Barbaro *et al.*, *Construction and Quality Control of Scintillator Tiles with WLS Fiber Readout for the 1995 CMS Test Beam Hadron Calorimeter*, University of Rochester preprint UR-1430, July 1995; H. Budd, *The CMS Central Hadron Calorimeter*, *Nucl. Phys. B*, (proc. suppl.) **B54** (1997) 191.
- [13] A. Bodek and P. Auchincloss, *Nucl. Instrum. Methods*, **A357** (1995) 292.
- [14] *The CMS Hadron Calorimeter Project Technical Design Report*, pp. 367-374, CERN/LHCC 97-31, CMS TDR 2, 20-Jun-1997 and references therein, p. 389.
- [15] D. Blomker *et al.*, *NIM*, **A311** (1992) 505.
- [16] J. Mainusch *et al.*, *NIM*, **A312** (1992) 451.
- [17] M. Bertoldi *et al.*, *Nucl. Instrum. Methods*, **A386** (1997) 301.
- [18] V. Abramov, *Nucl. Instrum. Methods A* **374** (1996) 34; V. Abramov, *Instruments and Experimental Techniques*, Vol. 40, **3** (1997) 318.
- [19] GEANT, Detector Description and Simulation Tool, CERN Program Library Long Writeup W5013. GEANT Version 3.21 is used with the default values for all parameters.
- [20] E. Auffray *et al.*, *Nucl. Instrum. Methods*, **A412** (1998) 223.
- [21] R. Wigmans *et al.*, *Nucl. Instrum. Methods*, **A259** (1987) 389; R. Wigmans *et al.*, *Nucl. Instrum. Methods*, **A265** (1988) 273.

[22] The correction for the longitudinal energy leakage for a finite length calorimeter is estimated using CCFR and NuTeV test beam measurements of hadron showers as a function of calorimeter depth. W. Sakumoto and L. de Barbaro, private communications.

[23] W. Sakumoto *et al.*, (CCFR Collaboration) *Nucl. Instrum. Methods*, **A294** (1990) 179.

[24] D. Harris, J. Yu, *et al.*, (NuTeV Collaboration), *Precision Calibration of the NuTeV Calorimeter*, University of Rochester preprint UR-1561, *Nucl. Instrum. Methods*, **A447** No.3, June 11, 2000. Note that CCFR and NuTeV used same iron-scintillator calorimeter.

[25] T.A. Gabriel and D. E. Groom, *Nucl. Instrum. Methods*, **A338** (1994) 336.

[26] P. de Barbaro *et al.*, *Test Beam Performance of the CDF Plug Upgrade Hadron Calorimeter*, Proceedings of the SCIFI97 Conference, Nov 4-11, 1997, Notre Dame, IN.

[27] Z. Ajaltouni *et al.*, *Nucl. Instrum. Methods*, **A387** (1997) 333.

[28] Atlas Tile Calorimeter Technical Design Report, CERN/LHCC 96-42, 15 December 1996.

[29] H. Fesefeldt, PITHA 85/02 (Aachen 1985)

[30] A. Fasso, A. Ferrari, J. Ranft and P. R. Sala, Proc. IV. Int. Conf. on Calorimetry at High Energy Physics, La Biodola (Is. d'Elba), Sept. 20-25, 1993, edited by A. Menzione and A. Scribano, World Scientific, p 493.

[31] C. Zeitnitz and T. A. Gabriel, *Nucl. Instrum. Methods*, **A349** (1994) 106.

[32] A. Farrai and P. R. Sala, ATLAS Internal Note, PHYS-No-086, June 1996.

Layer number	Absorber thickness	Scintillator thickness
ECAL 1-10	1.6 cm Pb	6 mm SCSN-38
HCAL 1-9	5 cm Cu	4 mm SCSN-81
HCAL 10-20	10 cm Cu	4 mm SCSN-81

Table 1

Longitudinal segmentation of ECAL and HCAL in the H2(1995) setup. Here a Pb-scintillator sampling calorimeter is used for the ECAL section.

Layer number	Absorber thickness	Scintillator thickness
HCAL 1	2 cm Cu	4 mm SCSN-81
HCAL 2-10	3 cm Cu	4 mm SCSN-81
HCAL 11-19	6 cm Cu	4 mm SCSN-81
HCAL 20	8 cm Cu + 29 cm Al	4 mm SCSN-81
HCAL 21	8 cm Cu	4 mm SCSN-81
HCAL 22	8 cm Cu	4 mm SCSN-81
HCAL 23	10 cm Cu	4 mm SCSN-81
HCAL 24	10 cm Cu	4 mm SCSN-81

Table 2

Longitudinal segmentation of HCAL in the H4(1995) setup. Here the ECAL module consists of a  $7 \times 7$  matrix of PbWO<sub>4</sub> crystals.

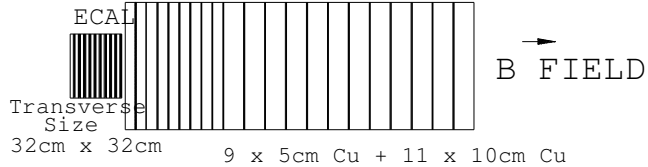
Layer number	Absorber thickness	Scintillator thickness
HCAL 1	2 cm Cu	4 mm SCSN-81
HCAL 2-7	3 cm Cu	4 mm SCSN-81
HCAL 8-21	6 cm Cu	4 mm SCSN-81
HCAL 22-27	8 cm Cu	4 mm SCSN-81

Table 3

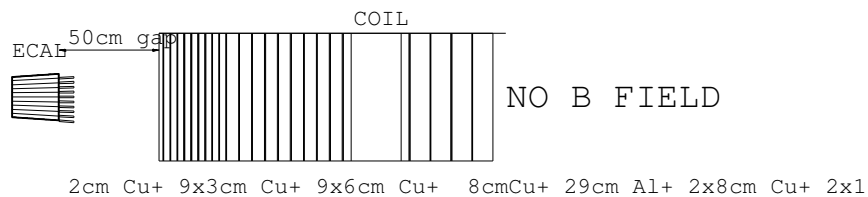
Longitudinal segmentation of HCAL in the H2(1996) setup. Here, the ECAL module consists of a  $7 \times 7$  matrix of  $\text{PbWO}_4$  crystals.

## CMS HCAL PROTOTYPES

H2 (1995) SETUP: Pb/Scin. ECAL MODULE



H4 (1995) SETUP: PbWO<sub>4</sub> CRYSTAL ECAL MODULE



H2 (1996) SETUP: PbWO<sub>4</sub> CRYSTAL ECAL MODULE

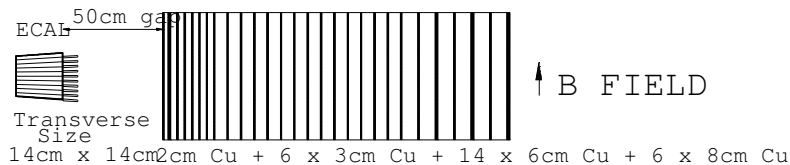


Fig. 1. Schematic drawing of the calorimeter modules used during the 1995 and 1996 tests in the H2 and H4 beamlines. A lead-scintillator sampling ECAL detector is used in the H2(1995) setup. A 7×7 matrix of PbWO<sub>4</sub> crystal ECAL is used in the H4(1995) and H2(1996) setups.

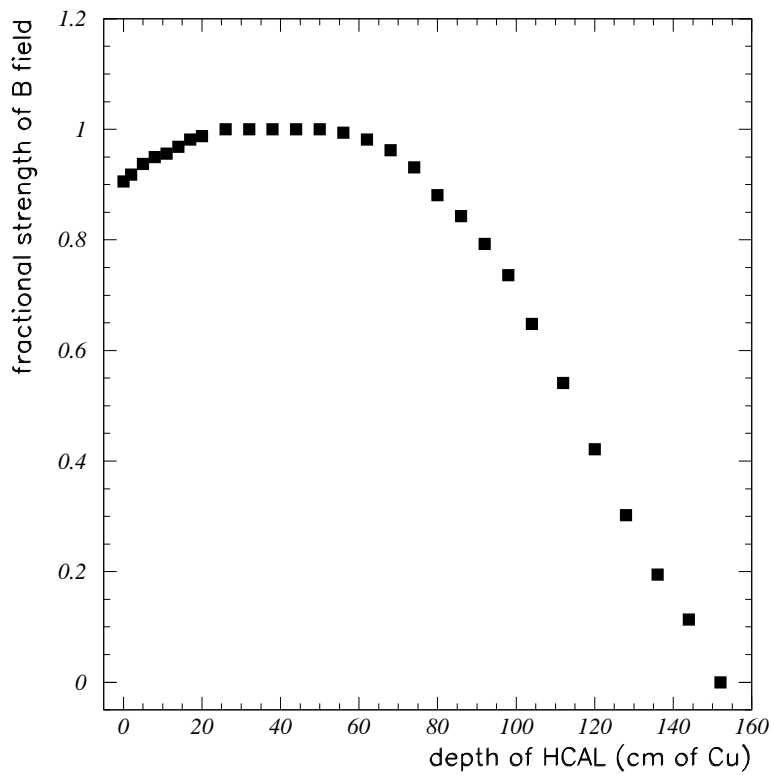


Fig. 2. Relative strength of the magnetic field, as a function of HCAL depth (in cm of Cu) for the CMS H2(1996) test beam run.

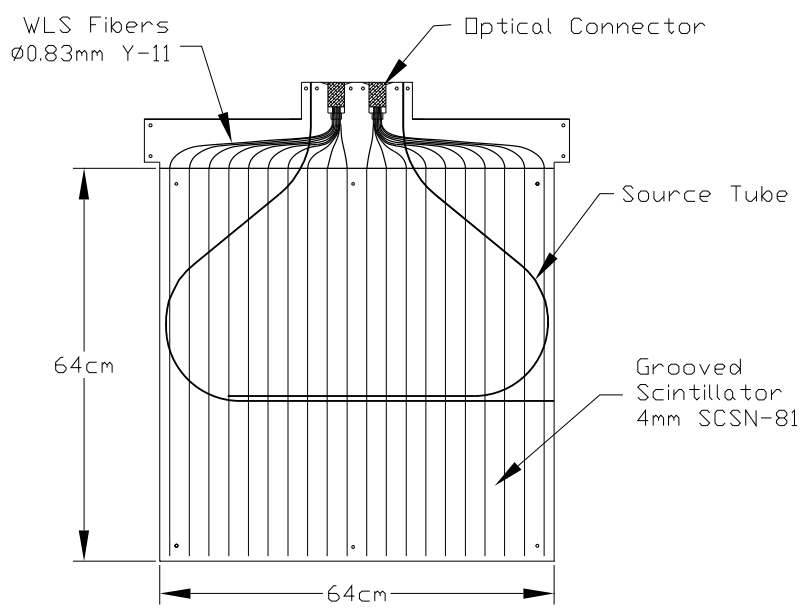


Fig. 3. Design of the 64 cm  $\times$  64 cm scintillator tile for the 1995 CMS Test Beam HCAL module.

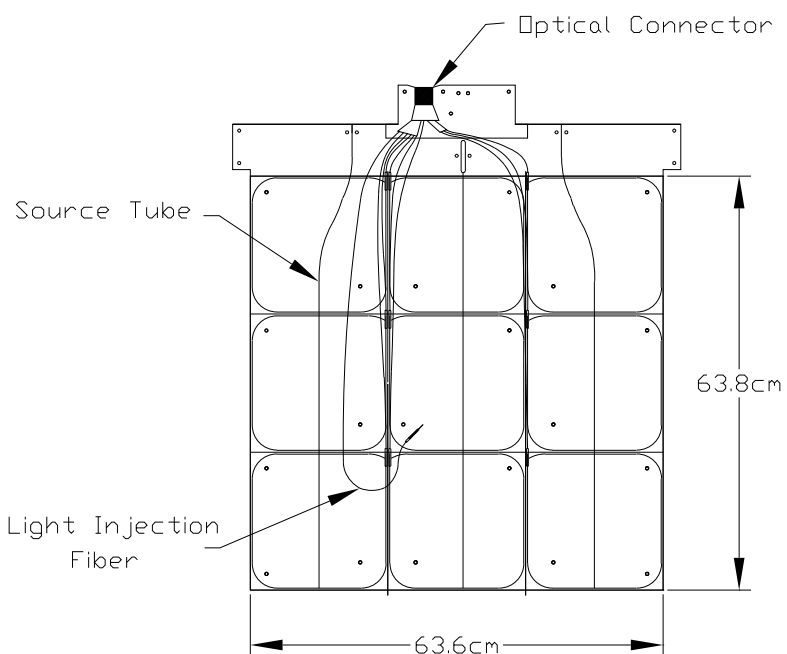


Fig. 4. Design of the 64 cm × 64 cm scintillator tile for the 1996 CMS Test Beam HCAL module.

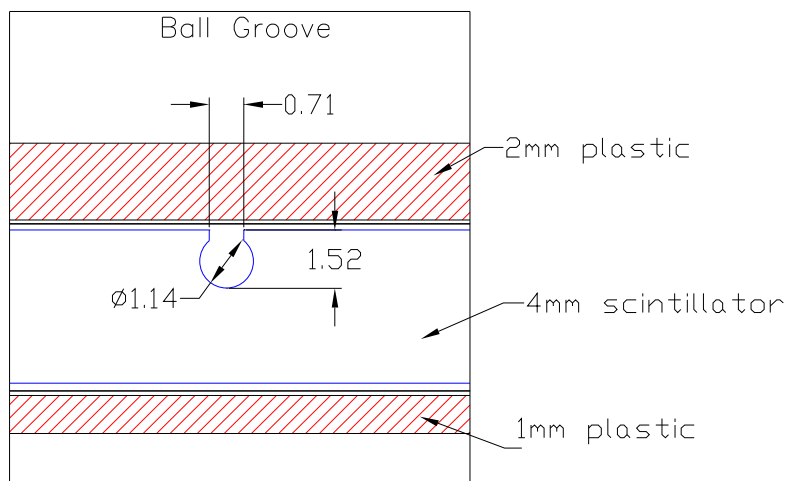


Fig. 5. Cross sectional view of the scintillator tile for the CMS Test Beam HCAL module. The dimensions in the drawing are shown in mm.

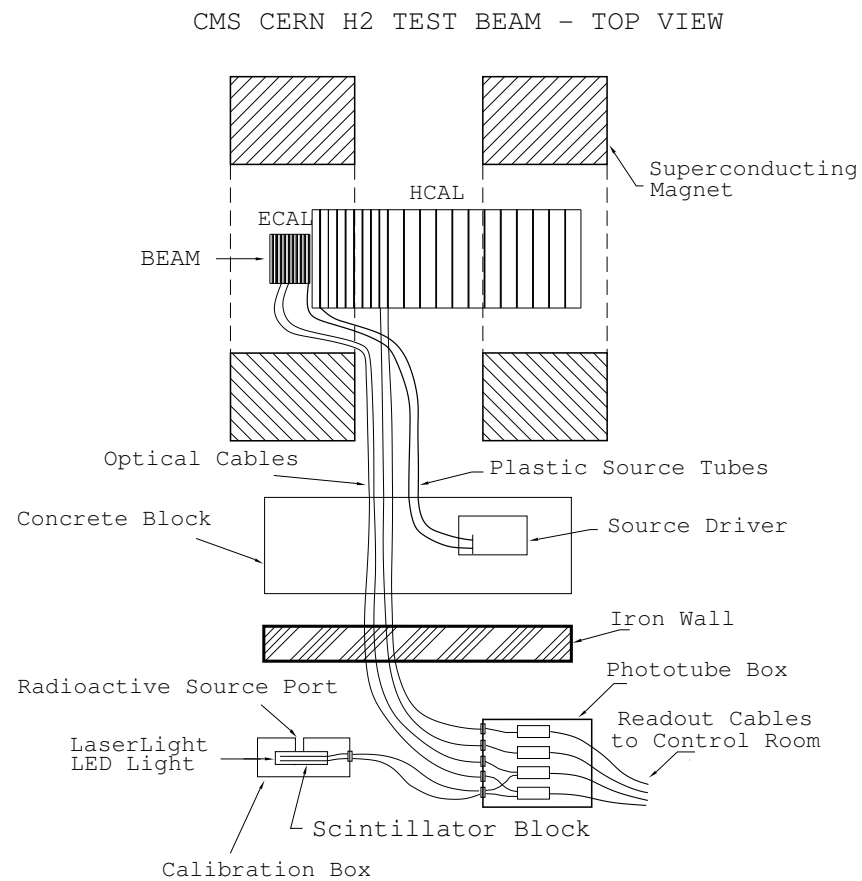


Fig. 6. Top view of the CMS test beam site at CERN H2 beamline. The drawing shows various calibration sub-systems.

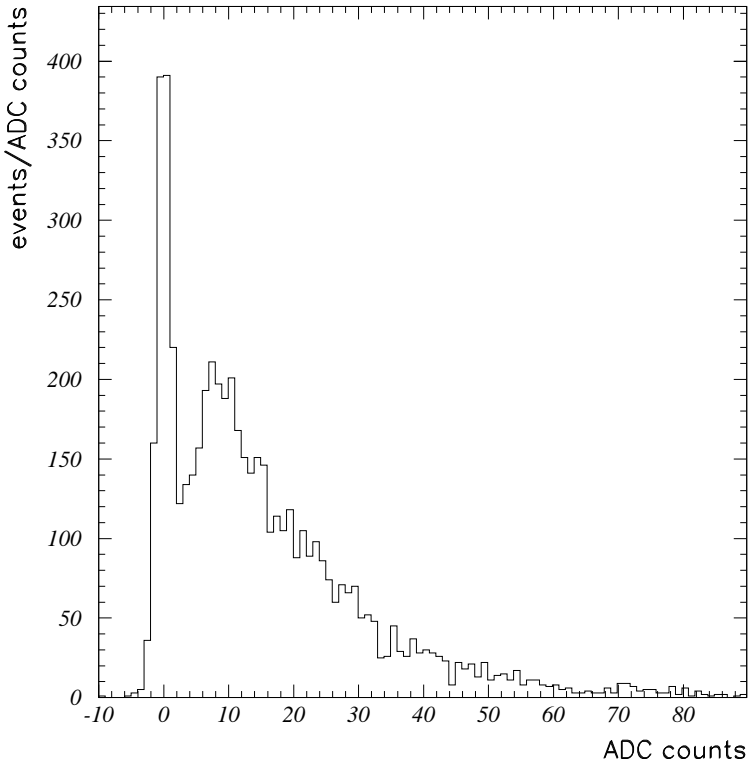


Fig. 7. H2(1995) data: ADC spectrum of 225 GeV/c muons in a single sampling scintillator layer. Based on the observed inefficiency of the layer of approximately 20%, the average number of photoelectrons per minimum ionizing particle per layer is 1.6 pe/mip.

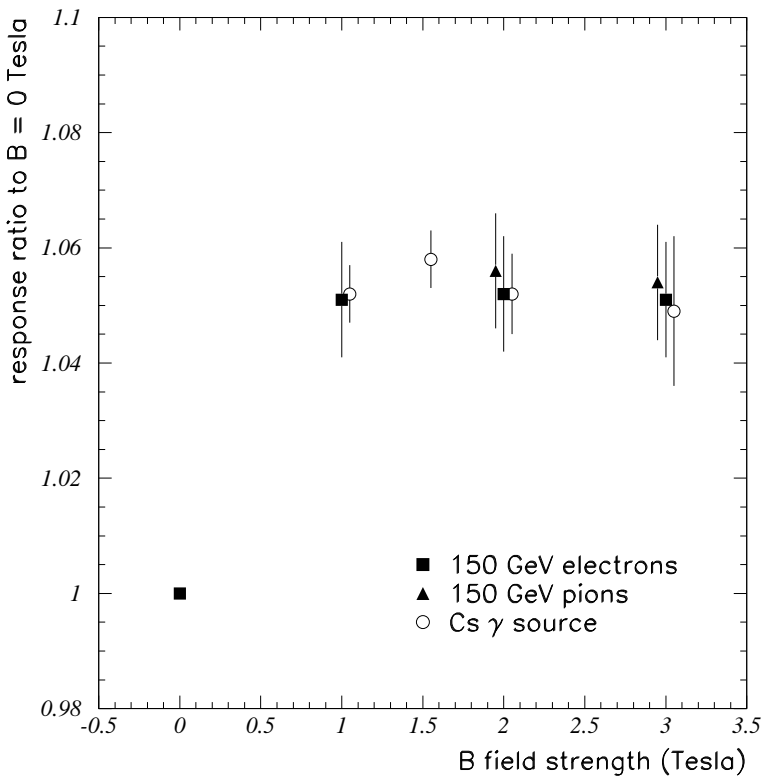


Fig. 8. H2(1995) data: average energy response of the tile/fiber calorimeter to pions and electrons as a function of B field, relative to response for B = 0 Tesla field. Also shown on the plot is the relative response of scintillator to radioactive gamma ray calibration source, as a function of B field. Here the B field lines are perpendicular to the scintillator plates (endcap configuration).

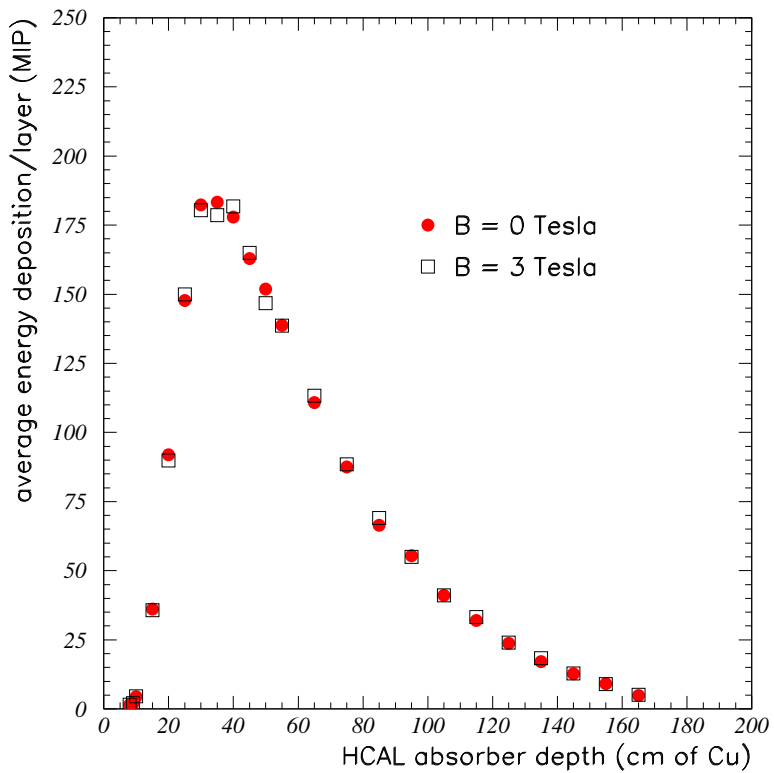


Fig. 9. H2(1995) data: comparison of 300 GeV/c pion shower profiles for  $B=0$  and  $B=3$  Tesla magnetic fields. The  $B$  field lines are perpendicular to the scintillator plates (endcap configuration). The pion shower profiles are divided by the average muon response for each layer, which corrects for the overall scintillator brightening effect.

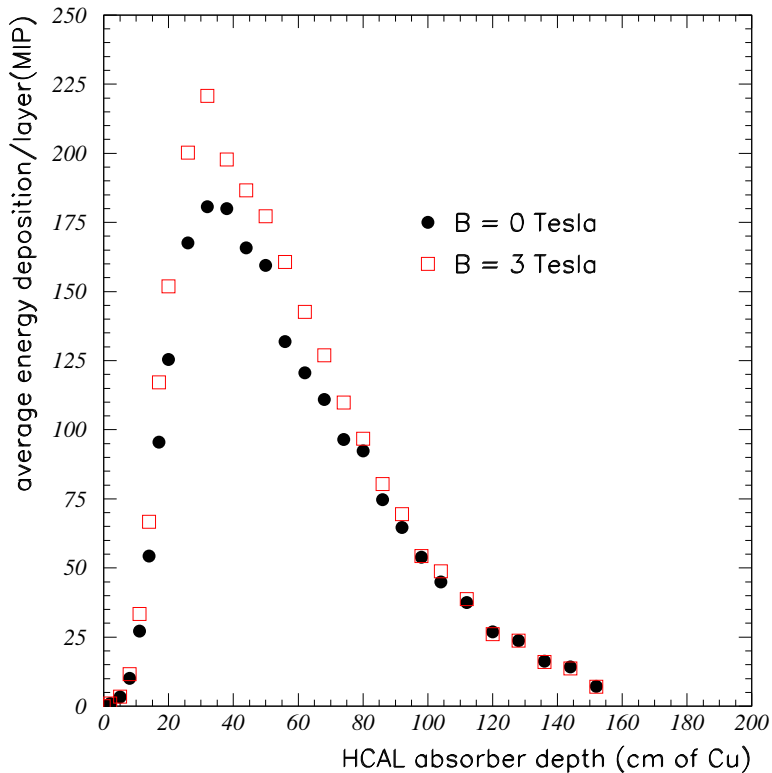


Fig. 10. H2(1996) data: comparison of 300 GeV/c pion shower profiles for  $B=0$  and  $B=3$  Tesla magnetic field. Here, the B field lines are parallel to the scintillator plates (barrel configuration). The pion shower profiles are divided by the average muon response for each layer, which corrects for the overall scintillator brightening effect.

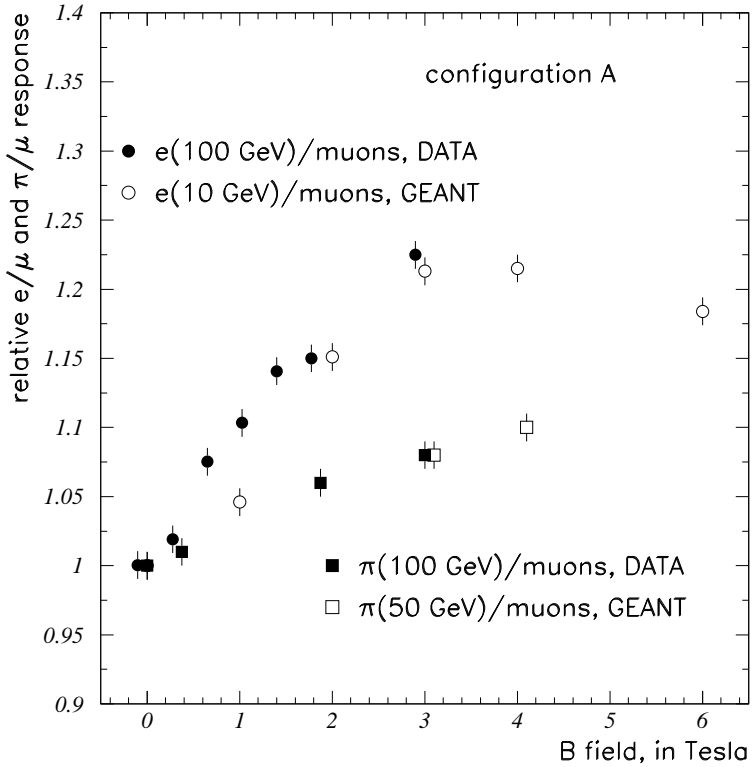


Fig. 11. H2(1996) data: effect of a B field on the average energy response of the tile/fiber calorimeter to pions and electrons divided by the average muon response. Response ratio is normalized to 1 for B= 0 Tesla. Also shown are the results from a GEANT simulation. Here, the B field lines are parallel to the scintillator plates (barrel configuration). The position of the scintillator package relative to the incident beam direction is the following: 1 mm plastic + 4 mm scintillator + 2 mm plastic (configuration A). The overall scintillator brightening B field effect is removed since the response of electrons and pions are divided by the average muon response in each layer.

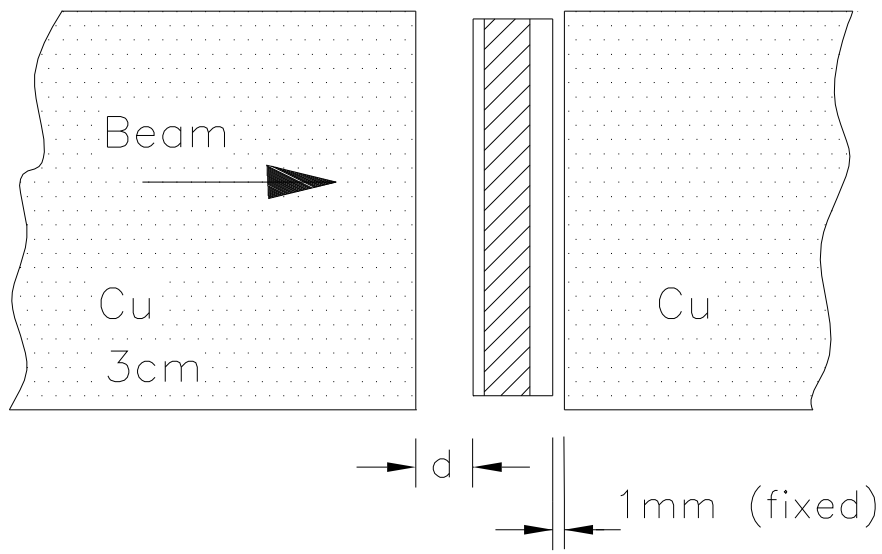


Fig. 12. Orientation of the scintillator package with respect to the beam direction inside the absorber gap (configuration A): 1 mm plastic + 4 mm scintillator + 2 mm plastic. The beam is incident from the left. In configuration B, the orientation of the package is reversed: 2 mm plastic + 4 mm scintillator + 1 mm plastic.

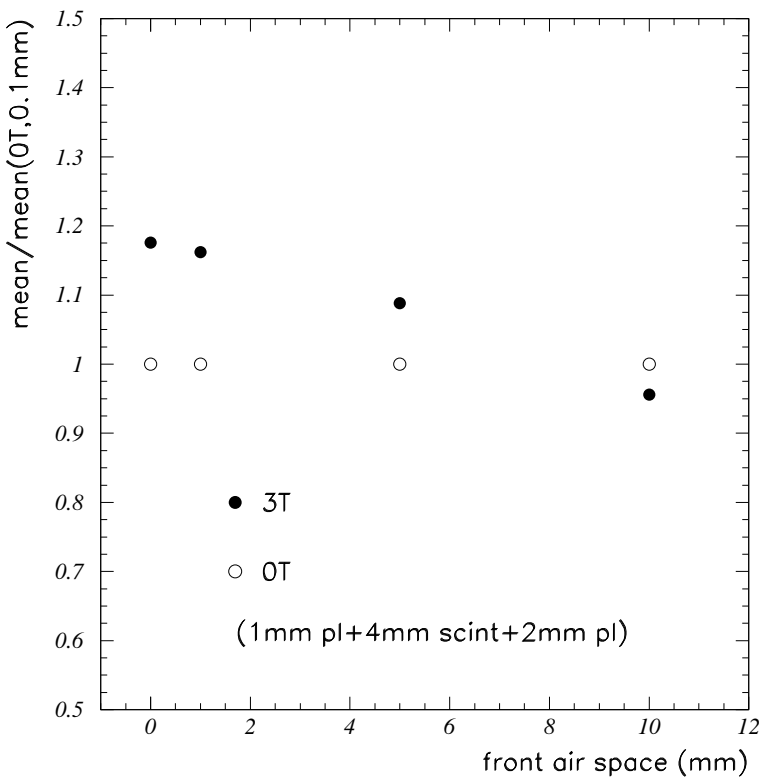


Fig. 13. Results of a GEANT simulation of the HCAL calorimeter response to 10 GeV electrons (in a 3 Tesla magnetic field parallel to the scintillator plates) as a function of the air gap (d) between the scintillator package and the most upstream absorber plate for configuration A.

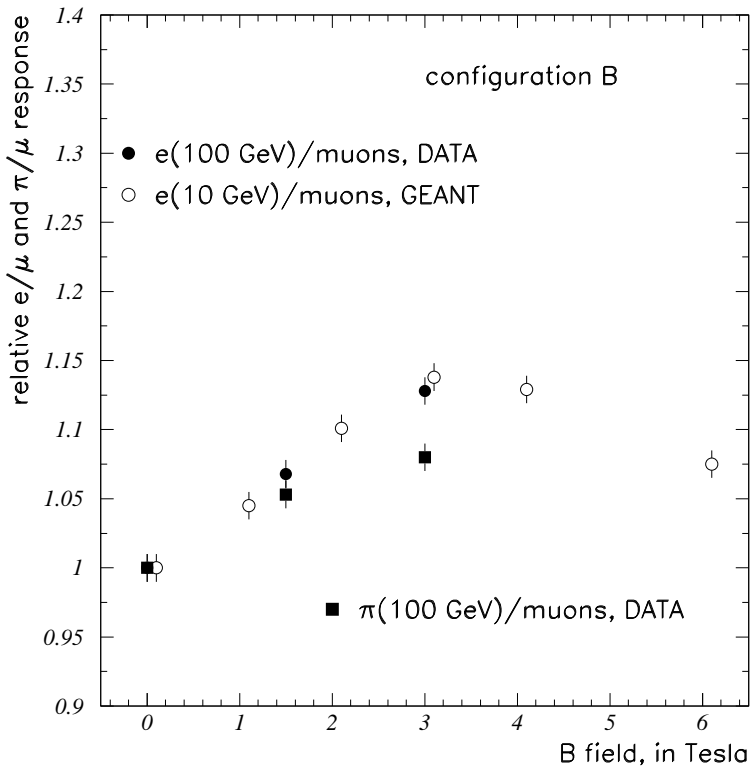


Fig. 14. H2(1996) data: effect of a B field on the average energy response of the tile/fiber calorimeter to electrons and pions. Response ratio is normalized to 1 for B= 0 Tesla. Also shown are results from GEANT simulation. Here, the B field lines are parallel to the scintillator plates (barrel configuration). The position of the scintillator package relative to the incident beam direction is as follows: 2 mm plastic + 4 mm scintillator + 1 mm plastic (configuration B). The overall scintillator brightening B field effect is removed since the response for electrons and pions is divided by the average muon response.

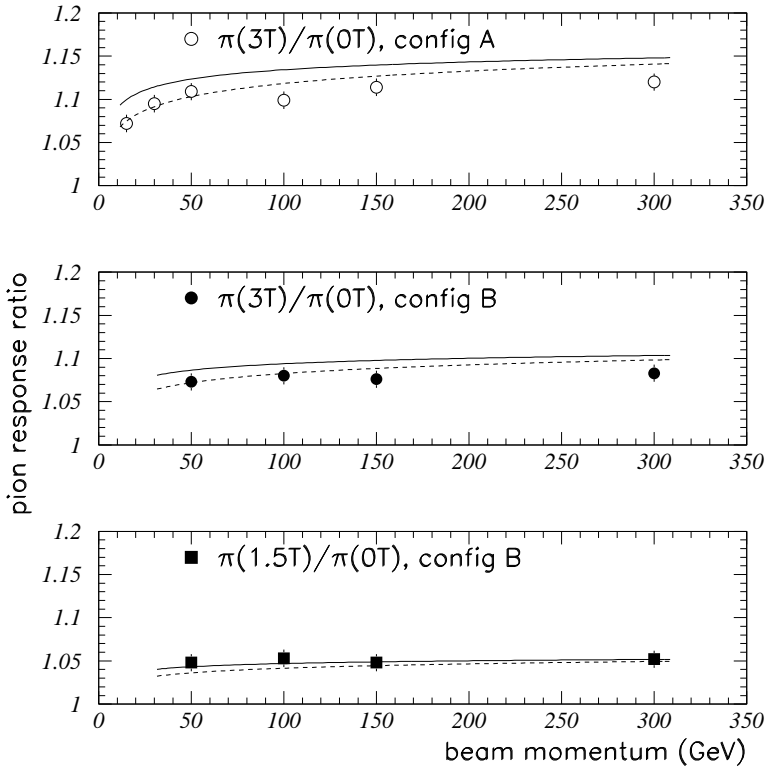


Fig. 15. H2(1996) data: the ratio of the pion response of HCAL at 3 Tesla and 1.5 Tesla to the pion response at 0 Tesla versus beam energy. Here, the B field lines are parallel to the scintillator plates (barrel configuration). The data is shown for two configurations of scintillator package inside absorber gap: 1 mm plastic + 4 mm scintillator + 2 mm plastic (configuration A) and 2 mm plastic + 4 mm scintillator + 1 mm plastic (configuration B). The lines correspond to the predictions using Groom (solid lines) and Wigmans (dashed lines) parametrizations of the fraction of the electromagnetic component in hadronic showers.

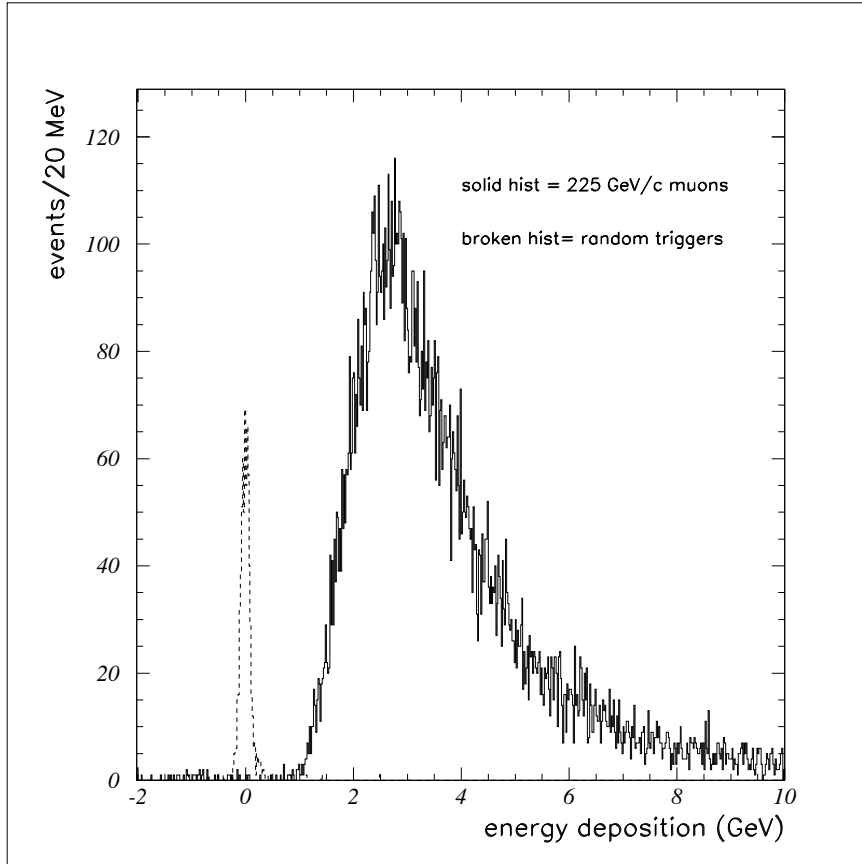


Fig. 16. H2(1995) data: energy deposited by 225 GeV/c muons in HCAL. The dashed line shows the energy reconstructed in HCAL for random triggers (pedestal events). The pedestal peak has a rms width of 80 MeV of equivalent hadron energy.

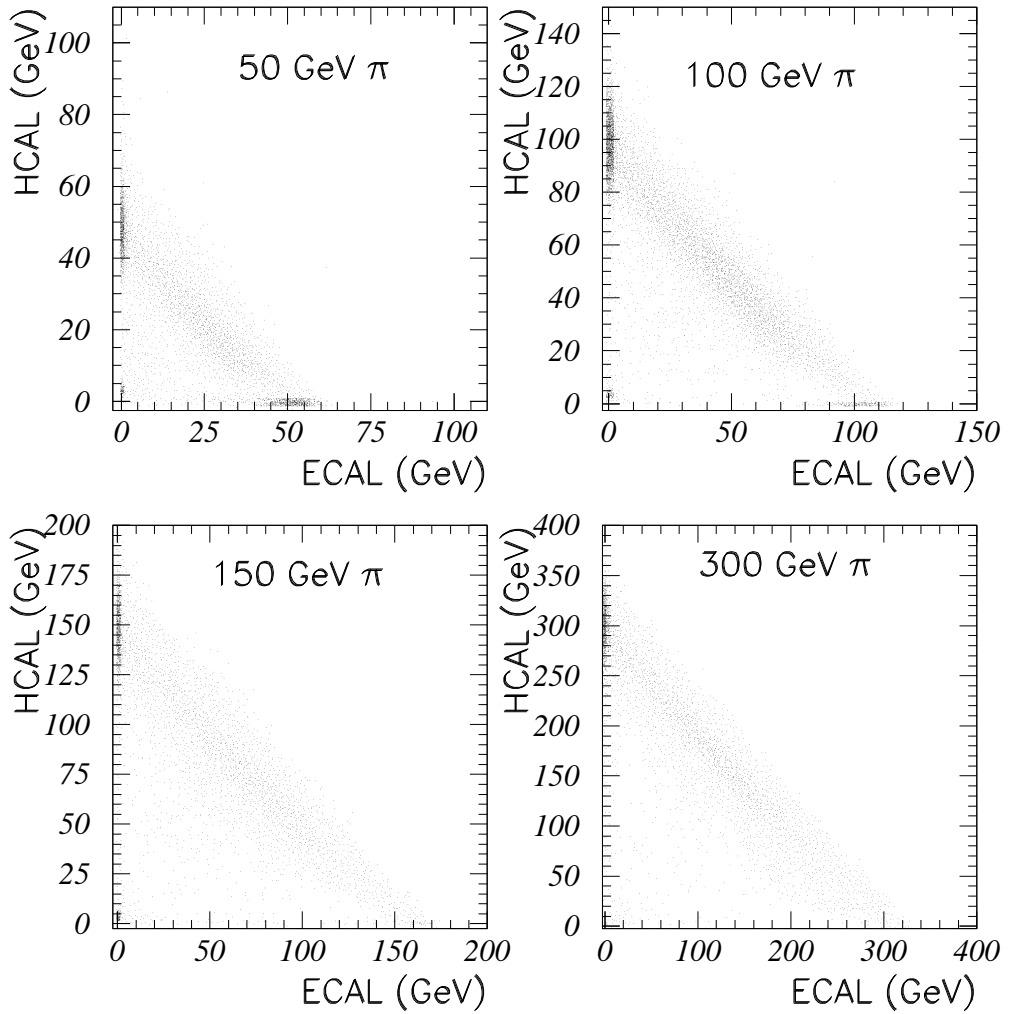


Fig. 17. H2(1995) data: scatter plots of  $E_{HCAL}$ , the energy deposited in the hadron compartment, (vertical scale) versus  $E_{ECAL}$ , the energy deposited in the Pb-scintillator electromagnetic compartment, (horizontal scale). In addition to pions, there is a contamination of electrons and muons in the beam.

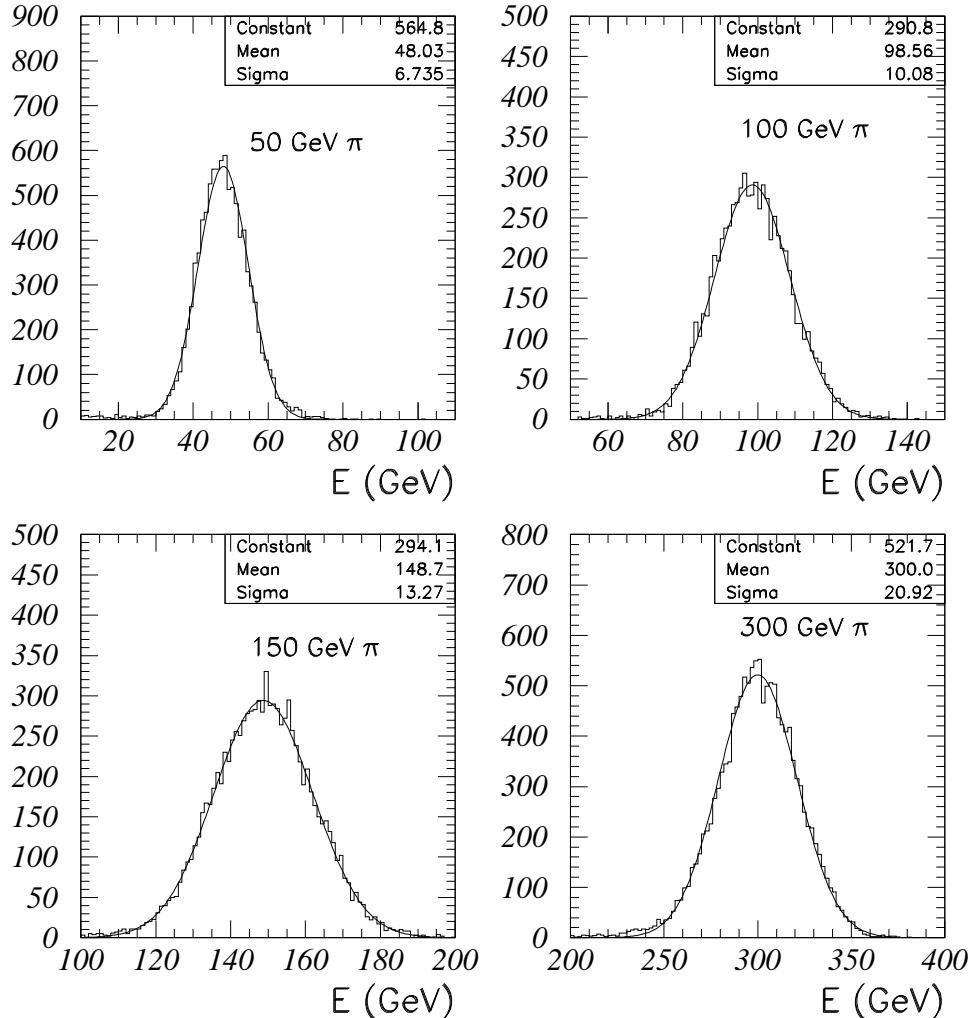


Fig. 18. H2(1995) data: reconstructed energy distributions for "mip-in-ECAL" pions. The minimum ionizing energy deposition in ECAL has been added to the energy sum.

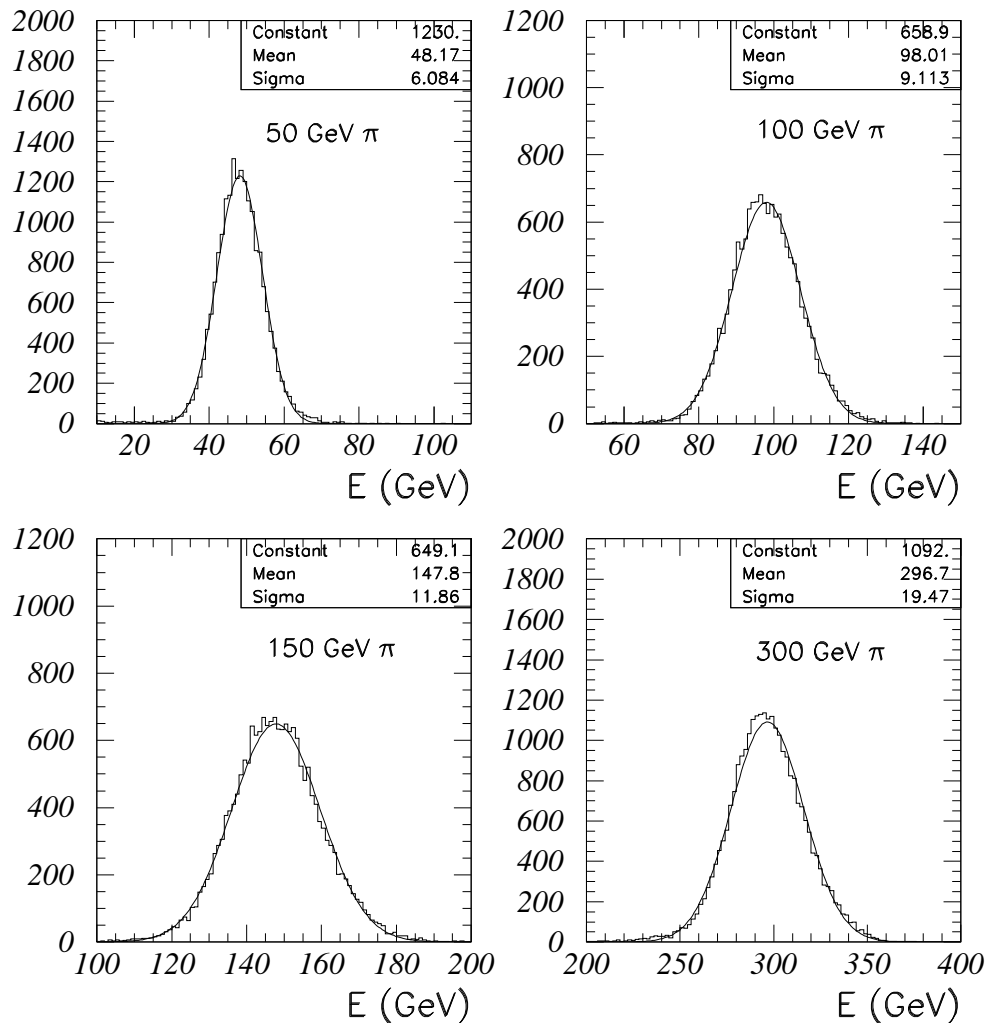


Fig. 19. H2(1995) data: distributions of  $E_{TOT}$ , the sum of energies deposited in the hadronic and electromagnetic compartment for "full pion sample".

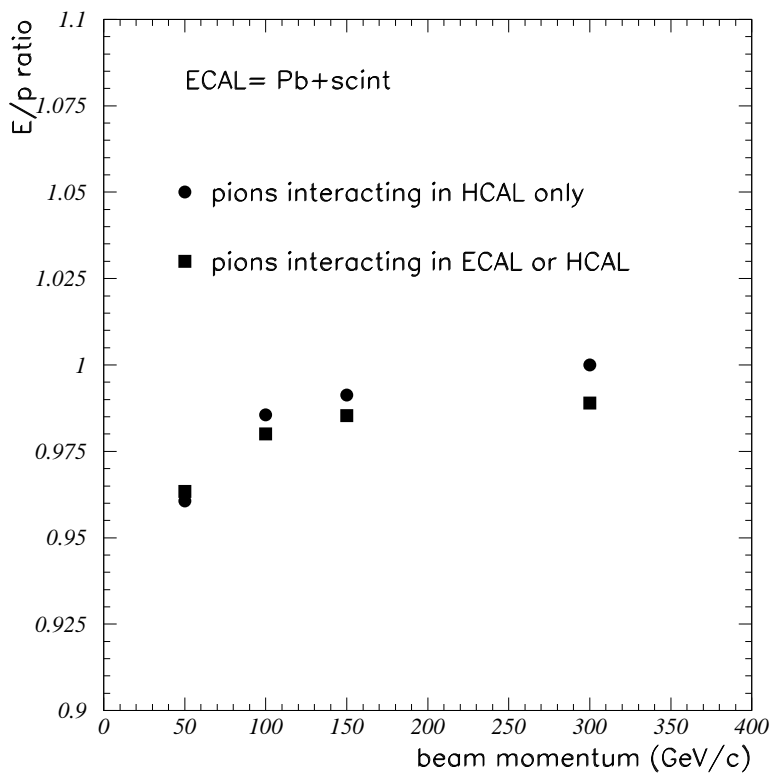


Fig. 20. H2(1995) data: linearity of the energy response for "mip-in-ECAL" pions and "full pion sample". The statistical errors are smaller than the size of the symbols.

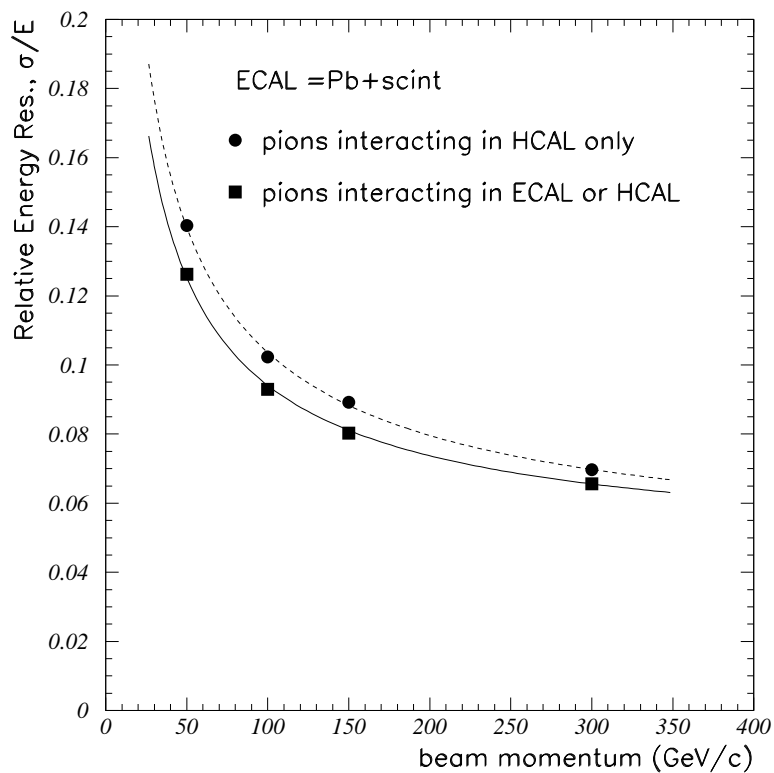


Fig. 21. H2(1995) data: fractional energy resolutions for "mip-in-ECAL" pions and "full pion sample". The statistical errors are smaller than the size of the symbols.

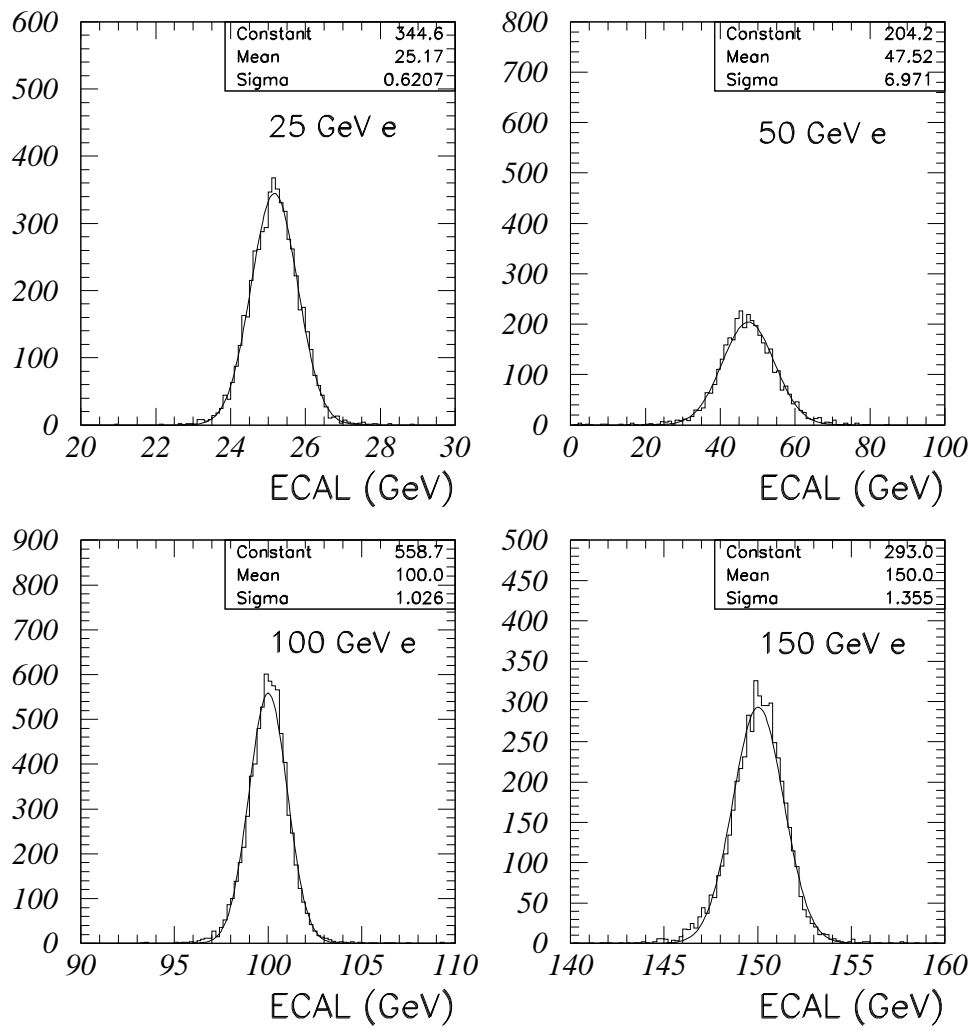


Fig. 22. H4(1995) data: response of the  $\text{PbWO}_4$  crystal ECAL calorimeter to 25, 50, 100 and 150  $\text{GeV}/c$  electrons.

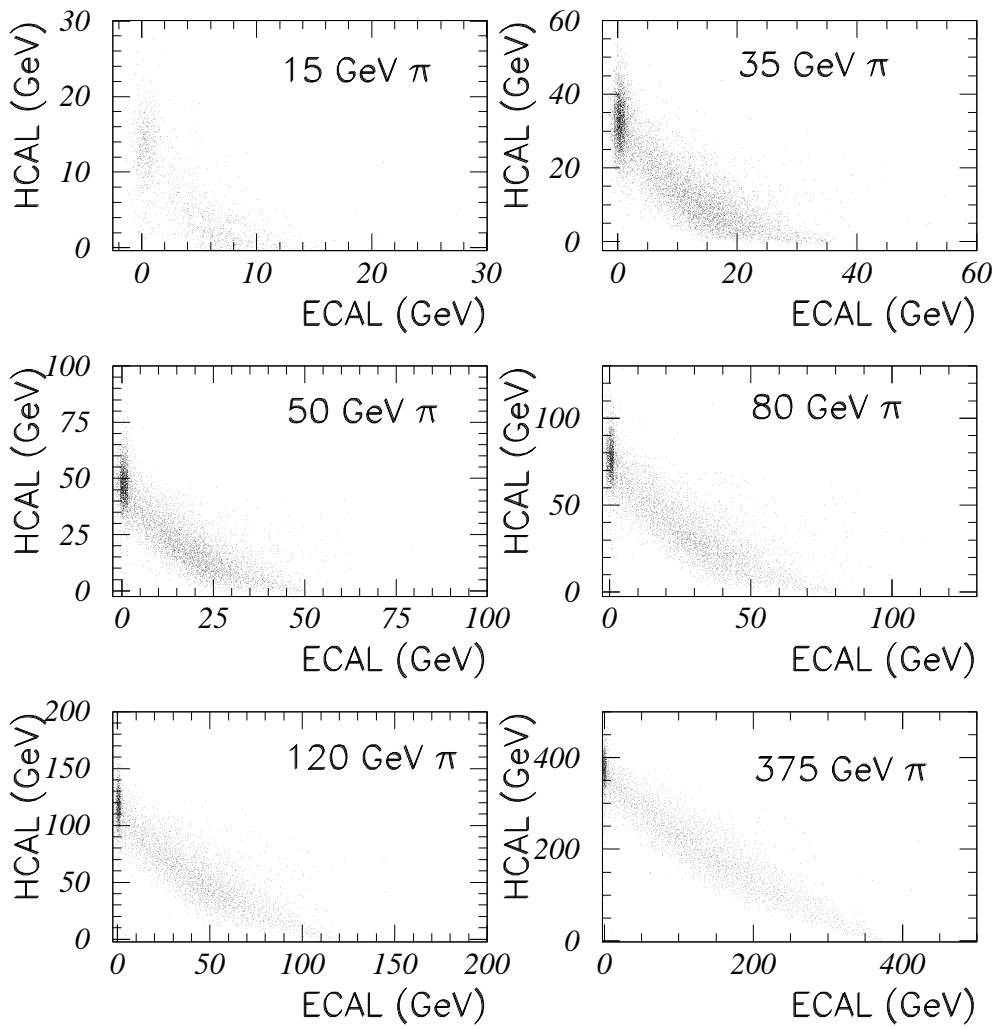


Fig. 23. H4(1995) data: scatter plots of the energy in HCAL versus the energy in the PbWO<sub>4</sub> crystal ECAL calorimeter for pions.

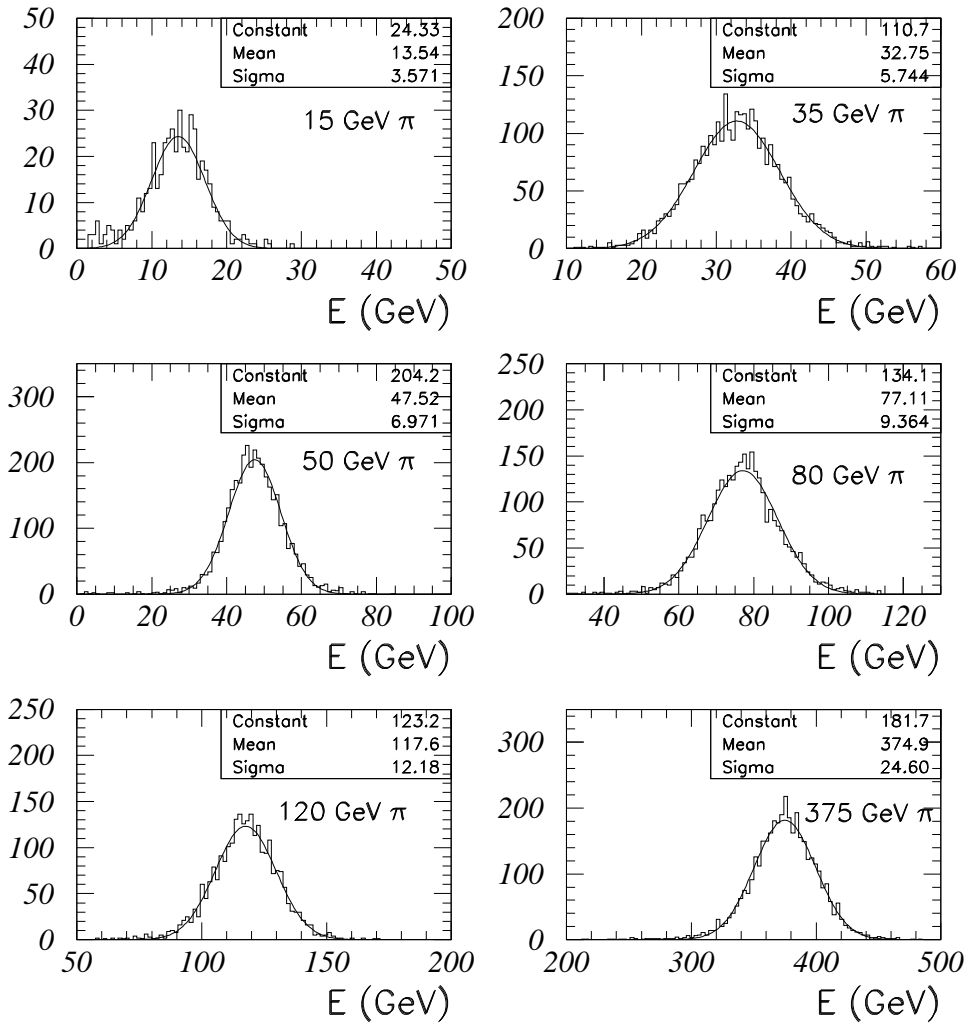


Fig. 24. H4(1995) data: the energy response of HCAL for "mip-in-ECAL" pions.

The minimum ionizing energy deposition in ECAL has been added to the energy sum.

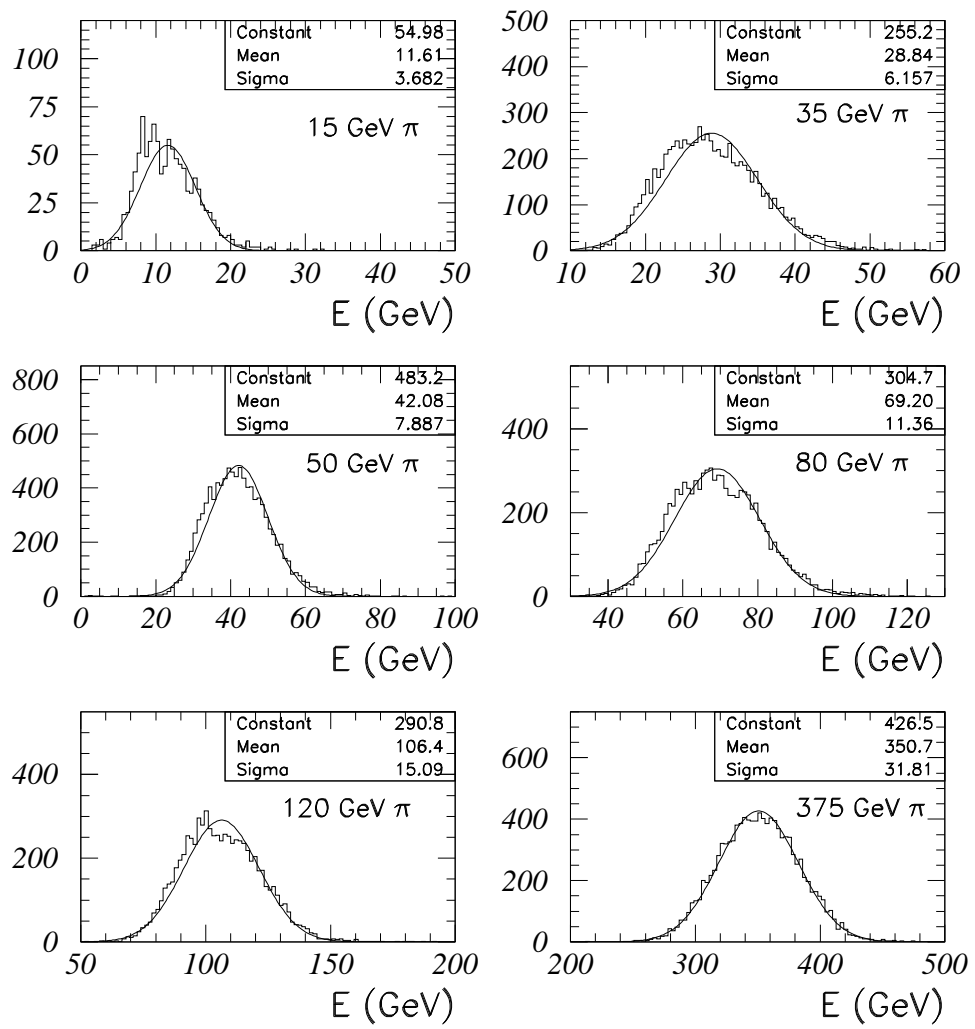


Fig. 25. H4(1995) data: the energy response of the combined crystal ECAL+HCAL calorimeter to "full pion sample".

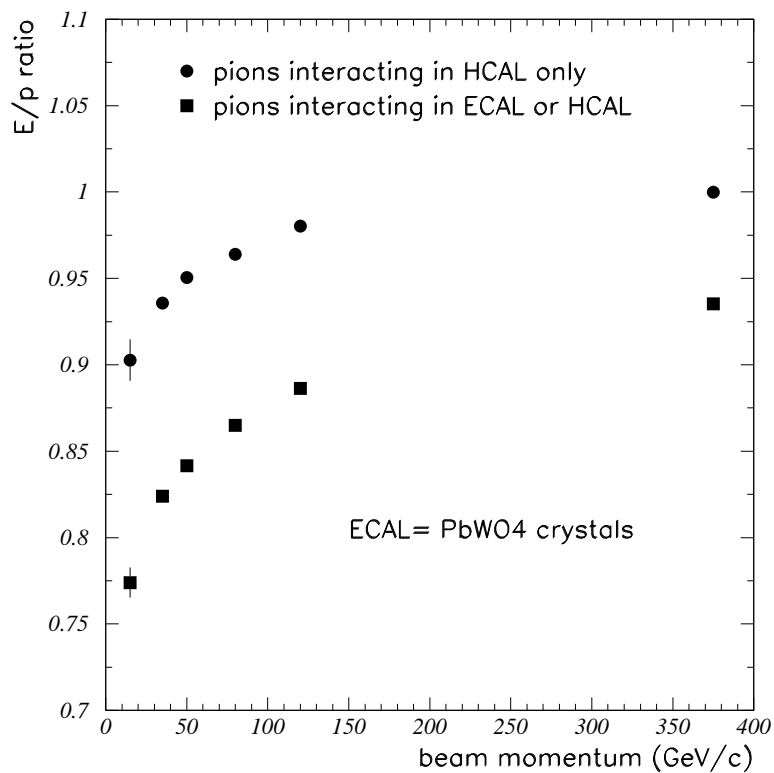


Fig. 26. H4(1995) data: linearity of the energy response for "mip-in-ECAL" and "full pion sample". The statistical errors for some of the data points are smaller than the symbol size.

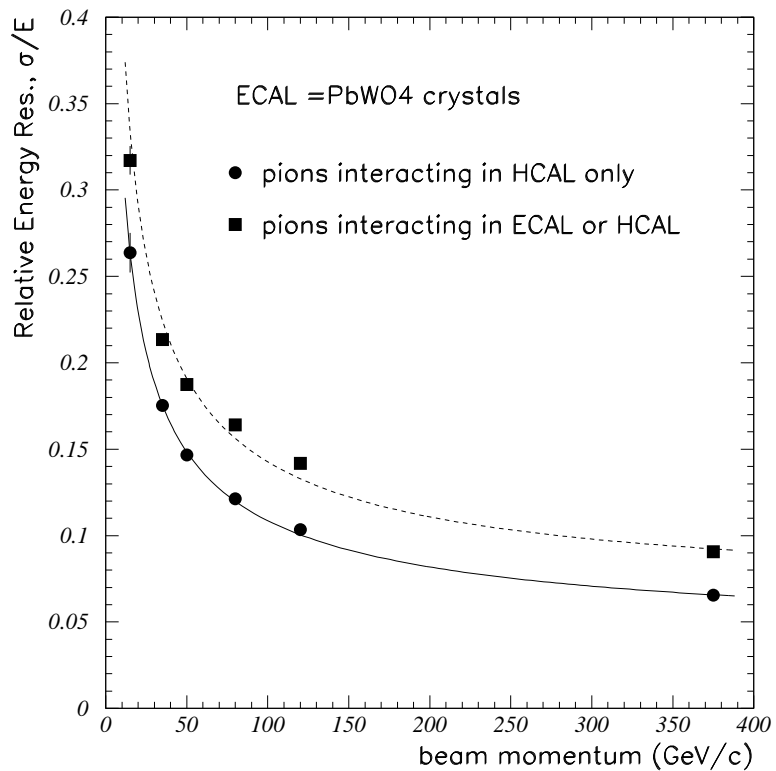


Fig. 27. H4(1995) data: fractional energy resolutions for "mip-in-ECAL" and "full pion sample". The statistical errors for some of the data points are smaller than the symbol size.

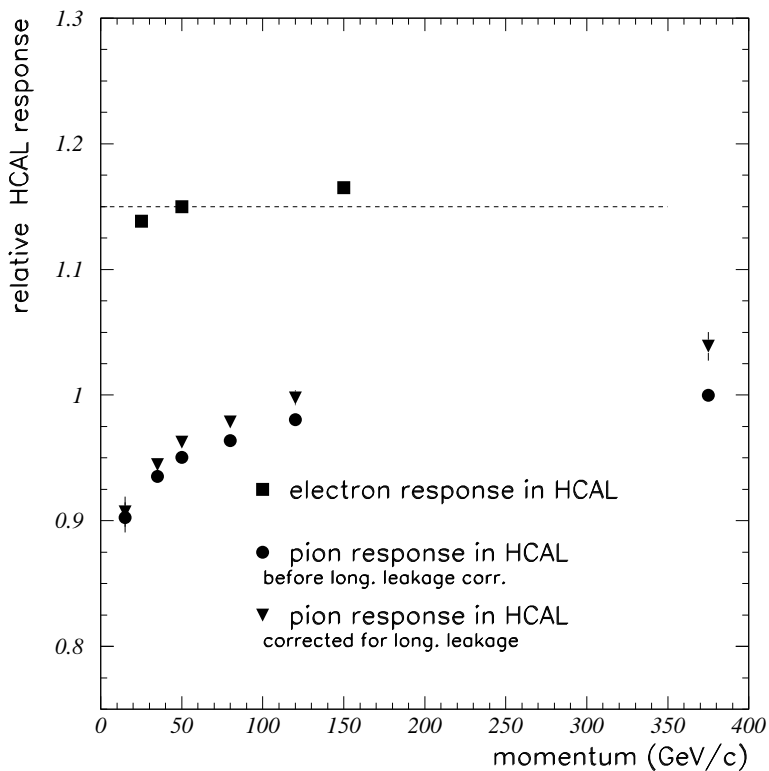


Fig. 28. H4(1995) data: the response of HCAL to electrons. The ECAL crystals are moved out of the beamline for these data. The figure also shows the response of HCAL to pions before and after a correction for downstream longitudinal energy leakage is applied. A 30% systematic uncertainty is assumed on the longitudinal leakage correction. The dotted line represents the ratio of the average electron response to the pion response at 375 GeV/c.

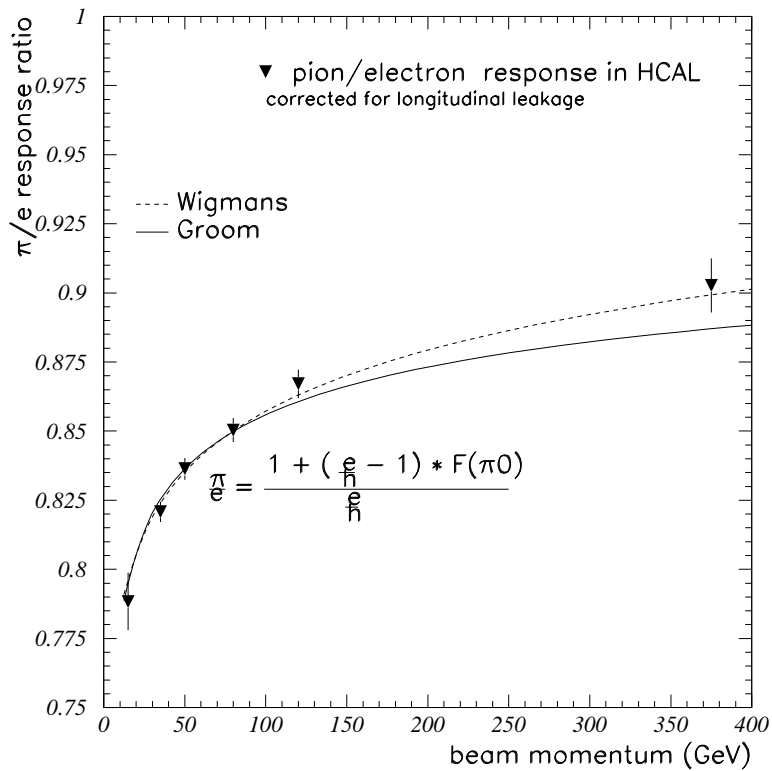


Fig. 29. H4(1995) data: the pion/electron response ratio for HCAL (only) as a function of beam momentum. The pion response of HCAL has been corrected for longitudinal leakage. We assume a linear electron response for HCAL (only), and use  $E(\text{ele})/E(\pi)=1.15\pm0.01$  at 375 GeV/c.

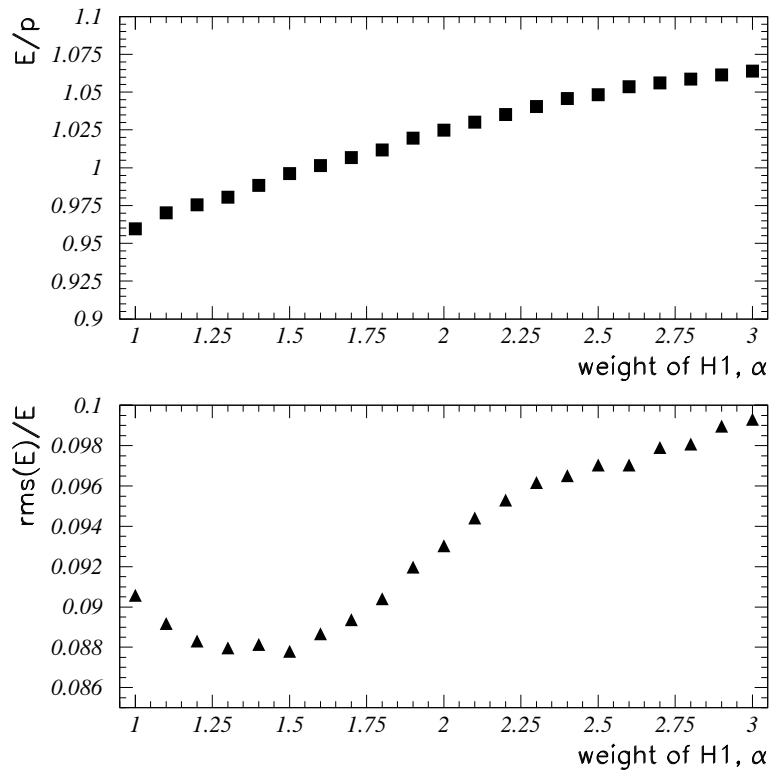


Fig. 30. H2(1996) data,  $B = 0$  Tesla data: the dependence of the  $E/p$  and the fractional rms energy resolution for 300 GeV/c pions as a function of parameter  $\alpha$ , the weight assigned to H1 (the first readout compartment of HCAL).

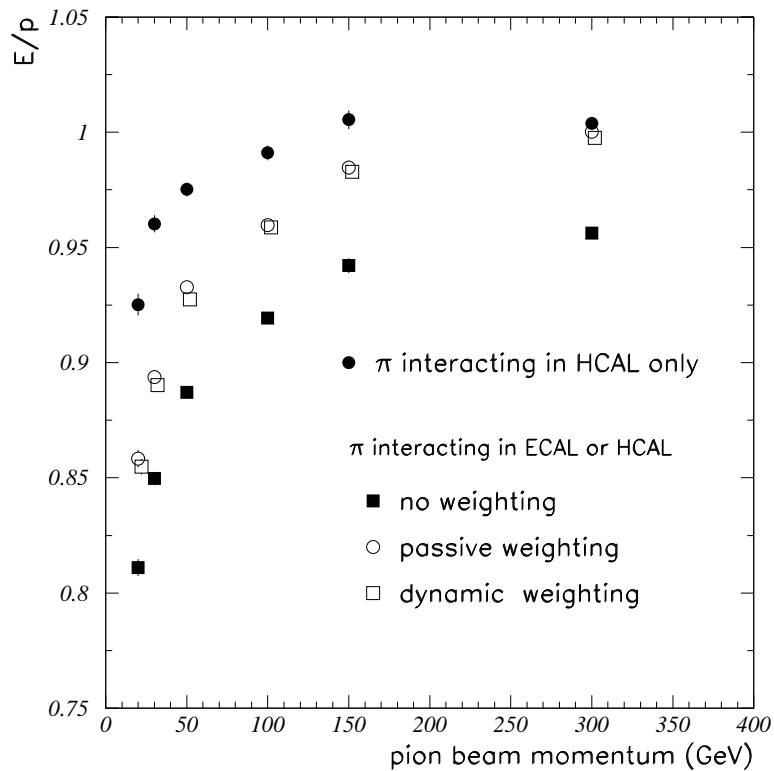


Fig. 31. H2(1996),  $B = 0$  Tesla data: the linearity of the response of HCAL to "mip-in-ECAL" pions and of the combined PbWO<sub>4</sub> crystal ECAL + HCAL system to "full pion sample" with  $\alpha=1.4$  and without the weighting of H1. The statistical errors are smaller than the size of the symbols.

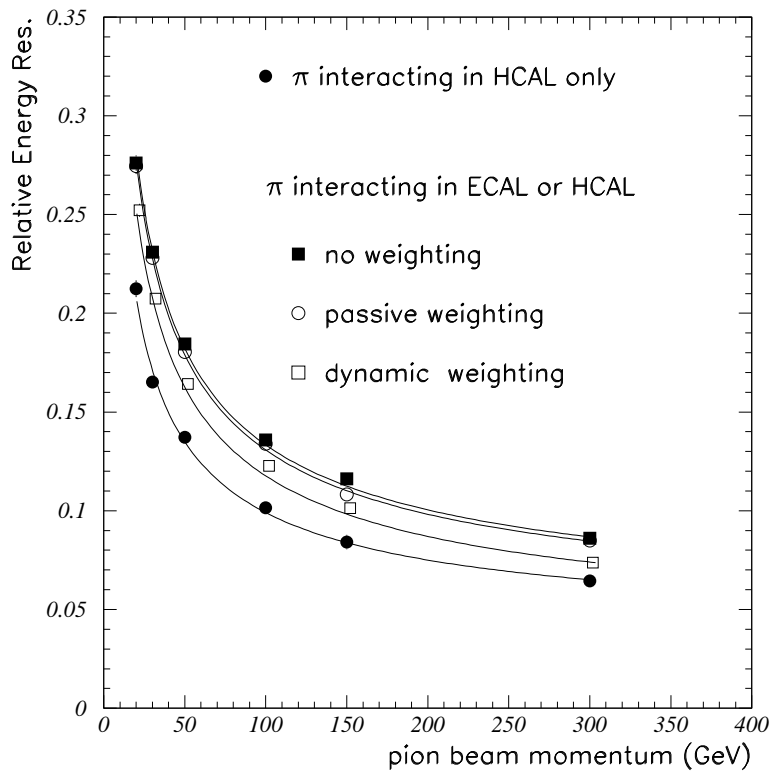


Fig. 32. H2(1996),  $B = 0$  Tesla data: the fractional pion energy resolution of HCAL to "mip-in-ECAL" pions and of the combined response of the  $\text{PbWO}_4$  crystal ECAL+HCAL system to "full pion sample" with  $\alpha=1.4$  and without the weighting of H1. The statistical errors are smaller than the size of the symbols.

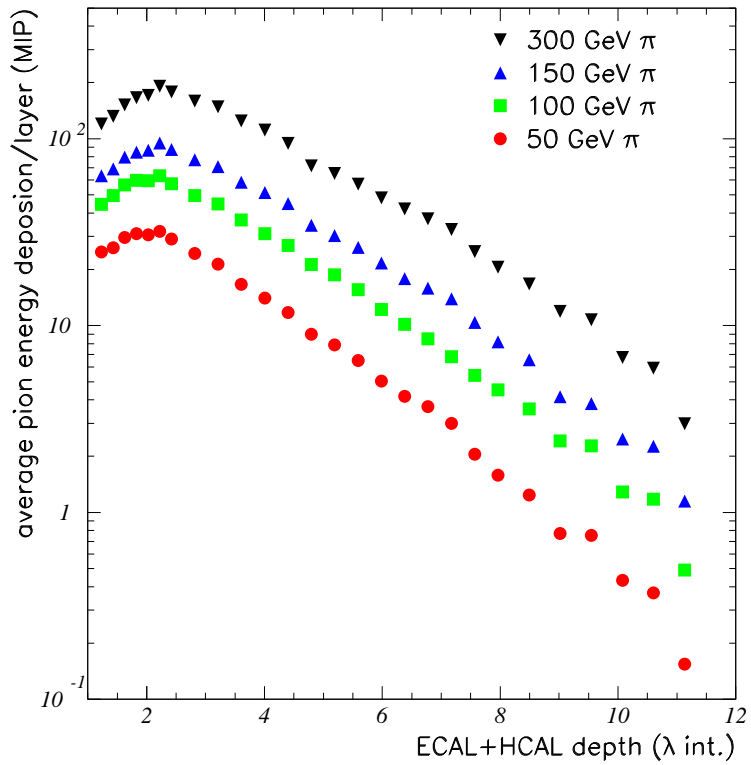


Fig. 33. H2(1996),  $B = 0$  Tesla data: average hadron shower profiles for 50, 100, 150 and 300 GeV/c pions as a function of calorimeter absorber depth. The total  $\lambda_{INT}$  includes the contribution of ECAL.

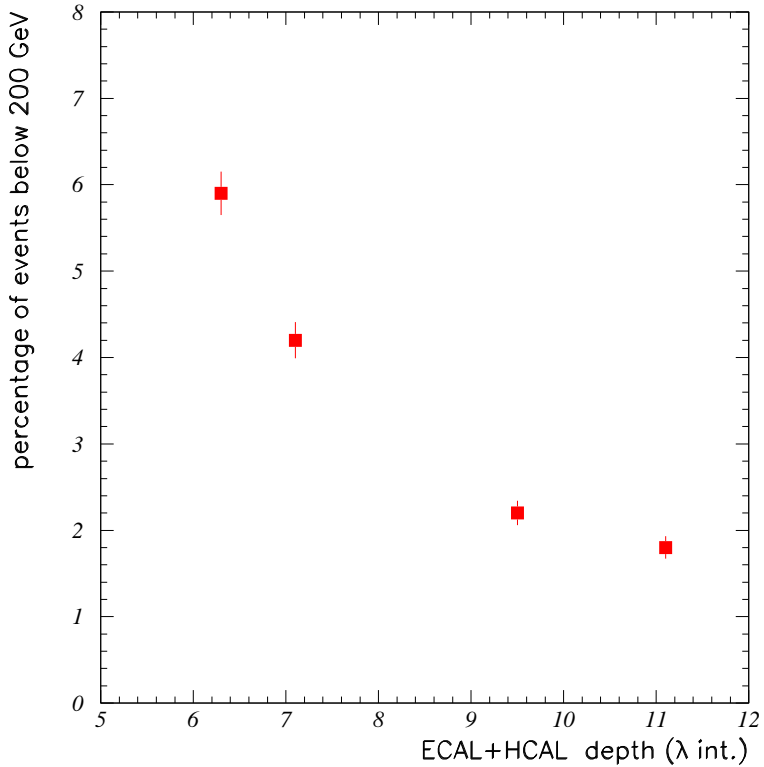


Fig. 34. H2(1996) data,  $B = 3$  Tesla: the fraction of 300 GeV/c pions with reconstructed energy less than 200 GeV (approximately 3  $\sigma$  below the mean, or 100 GeV of missing energy) versus total absorber depth. The total  $\lambda_{INT}$  includes the contribution of ECAL.

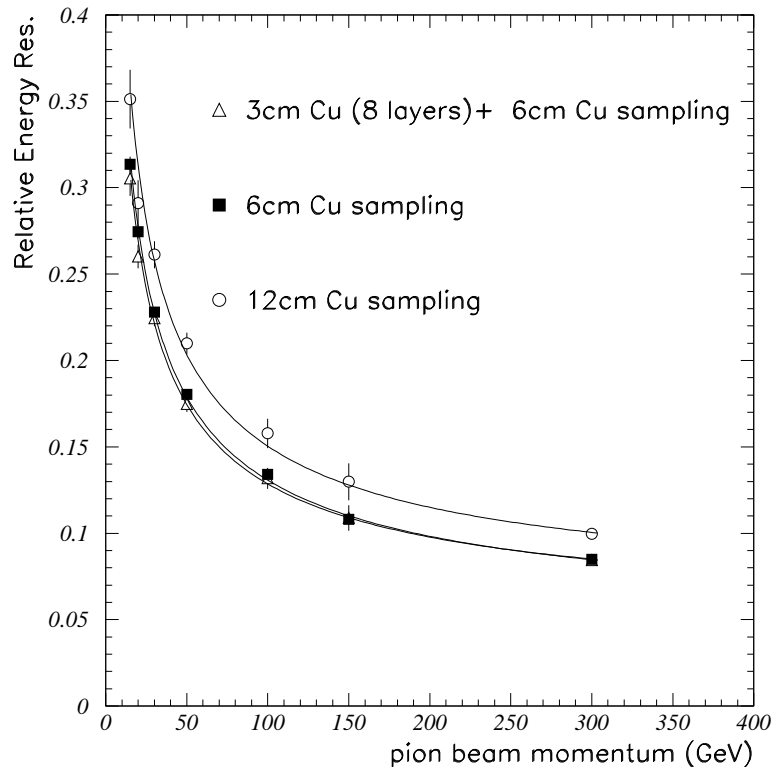


Fig. 35. H2(1996),  $B = 3$  Tesla data: comparison of the fractional pion energy resolution of the combined crystal ECAL+HCAL system, for various choices of absorber samplings in the inner HCAL:(a) 3 cm Cu sampling for first 8 layers, followed by 6 cm sampling, (b) 6 cm uniform sampling, and (c) 12 cm uniform sampling.

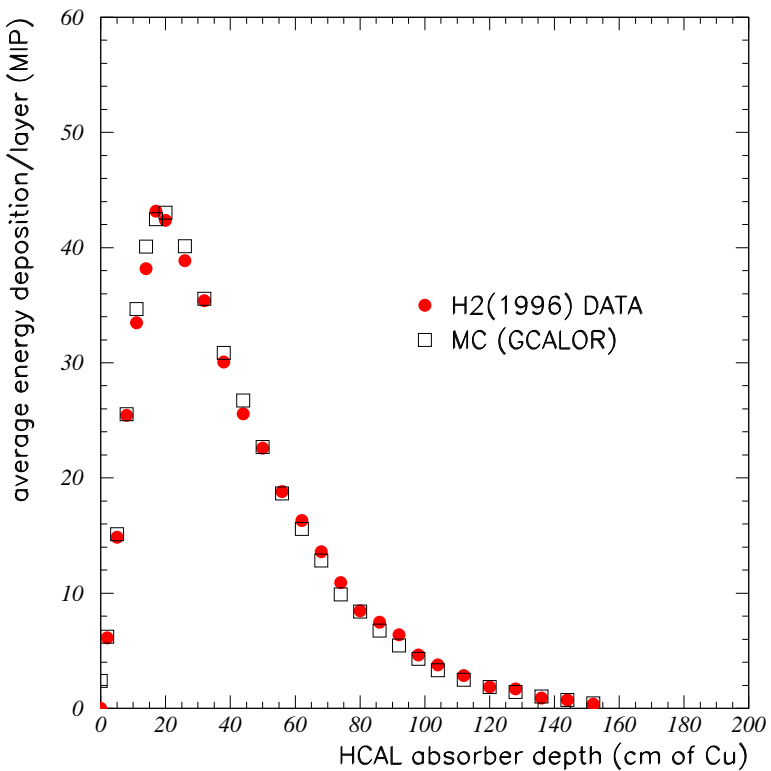


Fig. 36. Comparison of H2(1996),  $B = 0$  Tesla data with GEANT-GCALOR simulations for the average longitudinal shower profile of 50 GeV/c pions. The electromagnetic calorimeter has been taken out of the beamline.

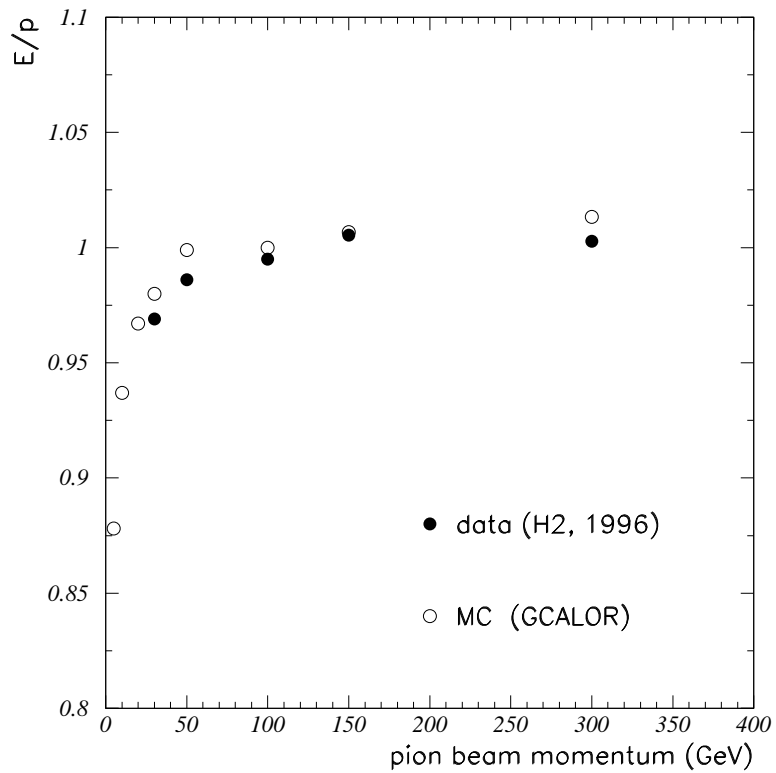


Fig. 37. H2(1996),  $B = 0$  Tesla data: linearity of the energy response of the hadron calorimeter (HCAL only) for pions and comparison with the GEANT-GCALOR MC simulation. The electromagnetic calorimeter has been taken out of the beamline.

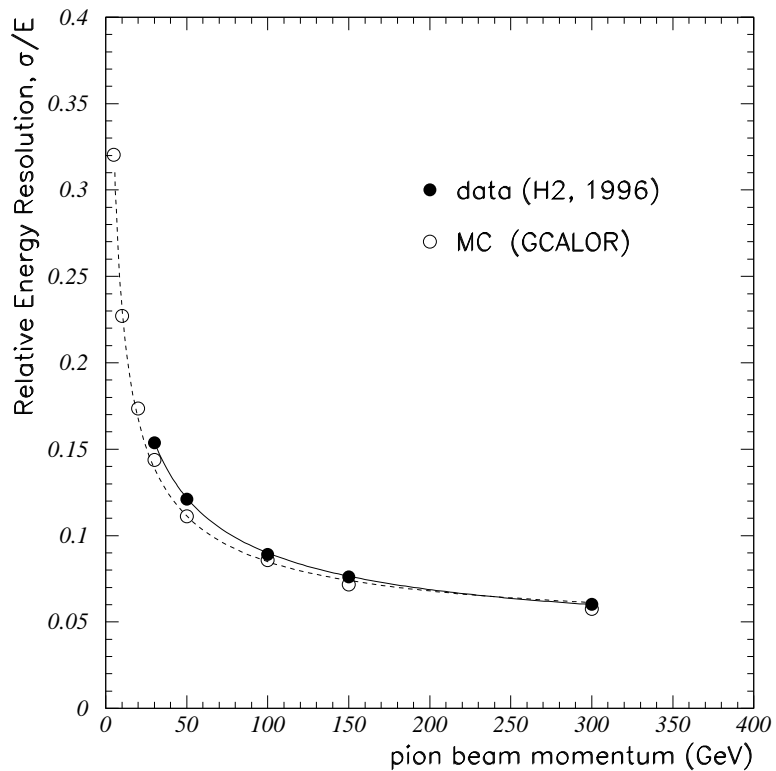


Fig. 38. H2(1996),  $B = 0$  Tesla data: the fractional energy resolution of the hadron calorimeter (HCAL only) for pions and comparison with the GEANT-GCALOR MC simulation. The electromagnetic calorimeter has been taken out of the beamline.

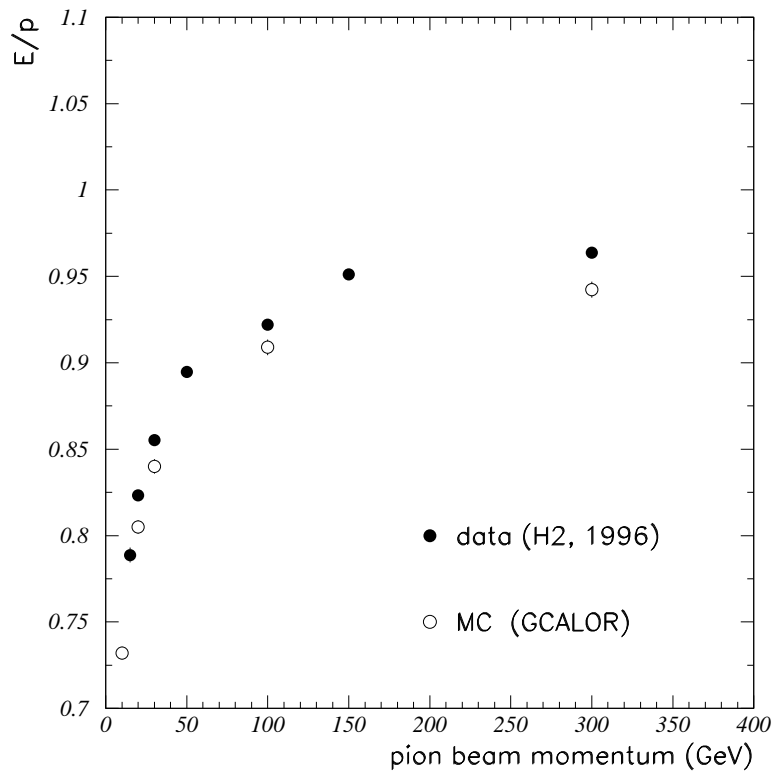


Fig. 39. H2(1996),  $B = 0$  Tesla data: the linearity of the energy response of the  $\text{PbWO}_4$  crystal ECAL+HCAL combined system for the "full pion sample" and comparison with the GEANT-GCALOR MC simulation.

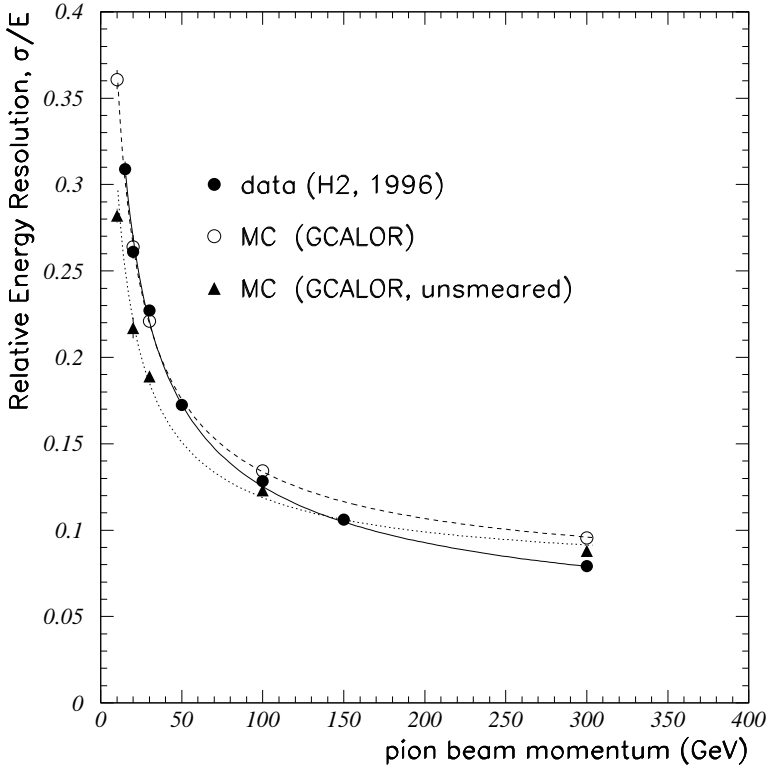


Fig. 40. H2(1996),  $B = 0$  Tesla data: the energy resolution of pions of the  $\text{PbWO}_4$  crystal ECAL+HCAL combined system for the "full pion sample" and comparison with the GEANT-GCALOR MC simulation. The MC simulation includes test beam detector effects (such as transverse leakage from prototype ECAL and ECAL electronics noise). Also shown (triangle symbols) is the MC simulation of the energy resolution of pions in crystal HCAL+ECAL combined system without these test beam detector effects (which are not expected to be present in the CMS experiment).

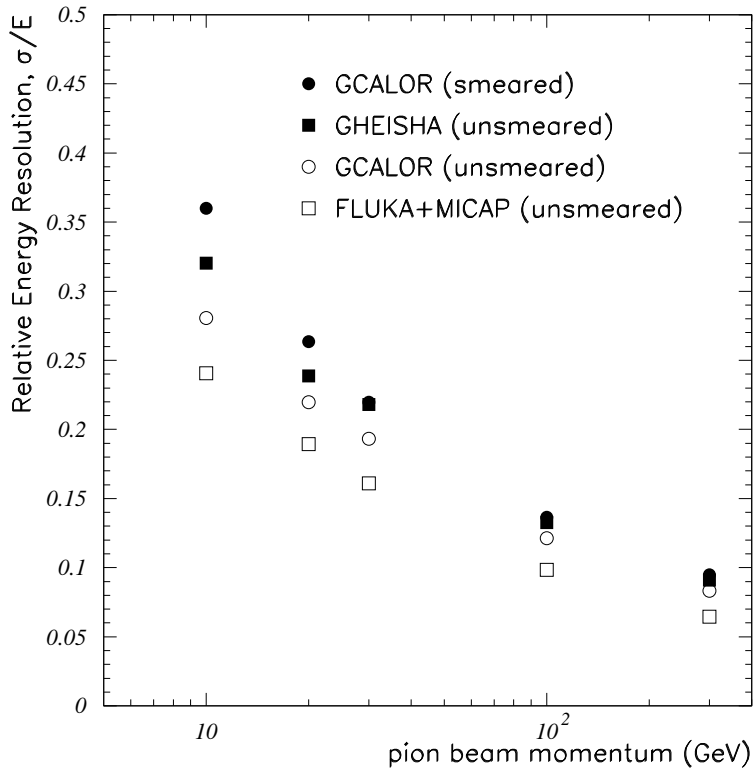


Fig. 41. Comparison of GEANT simulation for the pion energy resolution of the crystal ECAL+HCAL combined system using various generators (GHEISHA, GCALOR, and GFLUKA-MICAP) of hadron showers. The test beam data is represented best by the GCALOR simulation, which include all test beam detector effects and is labeled as "smeared". The GCALOR simulation labeled as "unsmeared" is expected to represent the experimental situation in the CMS experiment.